

# 1 Modeling the timing of Patagonian Ice Sheet retreat in the Chilean Lake District from 22- 2 10 ka

3  
4 Joshua Cuzzone<sup>1</sup>, Matias Romero<sup>2</sup>, Shaun A. Marcott<sup>2</sup>

5  
6 <sup>1</sup>Joint Institute for Regional Earth System Science and Engineering, University of California, Los  
7 Angeles

8 <sup>2</sup>Department of Geoscience, University of Wisconsin, Madison

9  
10 *Correspondence to:* Joshua K. Cuzzone (Joshua.K.Cuzzone@jpl.nasa.gov)

## 11 **Abstract**

12  
13 Studying the retreat of the Patagonian Ice Sheet (PIS) during the last deglaciation represents an  
14 important opportunity to understand how ice sheets outside the polar regions have responded to  
15 deglacial changes in temperature and large-scale atmospheric circulation. At the northernmost  
16 extension of the PIS during the last glacial maximum (LGM), the Chilean Lake District (CLD)  
17 was influenced by the southern westerly winds (SWW), which strongly modulated the hydrologic  
18 and heat budget of the region. Despite progress in constraining the nature and timing of deglacial  
19 ice retreat across this area, considerable uncertainty in the glacial history still exists due to a lack  
20 of geologic constraints on past ice margin change. Where the glacial chronology is lacking, ice  
21 sheet models can provide important insight into our understanding of the characteristics and drivers  
22 of deglacial ice retreat. Here we apply the Ice Sheet and Sea-level System Model (ISSM) to  
23 simulate the LGM and last deglacial ice history of the PIS across the CLD at high spatial resolution  
24 (450 meters). We present a transient simulation of ice margin change across the last deglaciation  
25 using climate inputs from the CCSM3 Trace-21ka experiment. At the LGM, the simulated ice  
26 extent across the CLD agrees well with the most comprehensive reconstruction of PIS ice history  
27 (PATICE). Coincident with deglacial warming, ice retreat ensues after 19ka, with largescale ice  
28 retreat occurring across the CLD between 18 and 16.5 ka. By 17 ka the northern portion of the  
29 CLD becomes ice free, and by 15 ka, ice only persists at high elevations as mountain glaciers and  
30 small ice caps. Our simulated ice history agrees well with PATICE for early deglacial ice retreat  
31 but diverges at and after 15 ka, where the geologic reconstruction suggests persistence of an ice  
32 cap across the southern CLD until 10 ka. However, given the high uncertainty in the geologic  
33 reconstruction of the PIS across the CLD during the later deglaciation, this work emphasizes a  
34 need for improved geologic constraints on past ice margin change. While deglacial warming drove  
35 the ice retreat across this region, sensitivity tests reveal that modest variations in wintertime  
36 precipitation (~10%) can modulate the pacing of ice retreat by up to 2 ka, which has implications  
37 when comparing simulated outputs of ice margin change to geologic reconstructions. While we  
38 find that TraCE-21ka simulates large-scale changes in the SWW across the CLD that are consistent  
39 with regional paleoclimate reconstructions, the magnitude of the simulated precipitation changes  
40 is smaller than what is found in proxy records. From our sensitivity analysis we can deduce that  
41 larger anomalies in precipitation as found in paleoclimate proxies may have had a large impact on  
42 modulating deglacial ice retreat, highlighting an additional need to better constrain the deglacial  
43 change in the strength, position, and extent of the SWW as it relates to understanding the drivers  
44 of deglacial PIS behavior.

46 **1 Introduction**

47

48 During the Last glacial maximum (LGM), the Patagonian Ice Sheet (PIS) covered the Andes  
49 mountains from 38°S to 55°S, with an estimated sea-level equivalent ice volume of 1.5 meters  
50 (Davies et al., 2020). At the northernmost extent of the PIS, across an area presently known as the  
51 Chilean Lake District (CLD: 37°S-41.5°S), the LGM to deglacial ice behavior and related climate  
52 forcings has been a subject of historical interest (Mercer, 1972; Porter, 1981; Lowell et al., 1995;  
53 Andersen et al., 1999; Denton et al., 1999; Glasser et al., 2008, Moreno et al., 2015; Kilian and  
54 Lamy, 2012; Lamy et al., 2010), and have served as important constraints towards understanding  
55 the drivers of ice sheet change across centennial to millennial timescales. Currently, PATICE  
56 (Davies et al., 2020) serves as the latest and most complete reconstruction of the entire PIS during  
57 the LGM and last deglaciation. Across the CLD (Figure 1), the LGM ice limits are only well  
58 constrained by terminal moraines in the southwest and western margins (Denton et al., 1999;  
59 Glasser et al., 2008, Moreno et al., 2015). However, due to a lack of geomorphological and  
60 geochronologic constraints on ice margin change following the LGM, the reconstructed  
61 deglaciation remains highly uncertain.

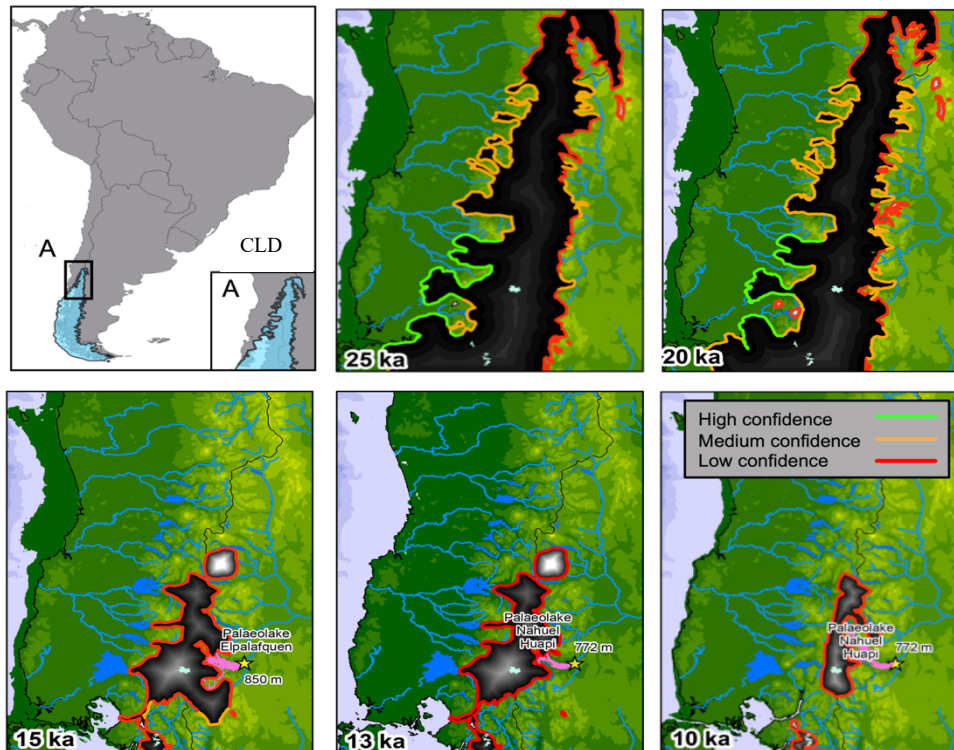


Figure 1. Location of the study area across the Chilean Lake District (CLD; Upper Left Panel). The reconstructed ice extent from PATICE for the PIS across the CLD at 25 ka, 20 ka, 15 ka, 13 ka, and 10 ka are taken from Davies et al., 2020. The color of the line marking the reconstructed ice extent corresponds to the confidence in the reconstruction as described in section 3.3.

62 While deglacial warming is a primary driver of ice retreat across the CLD, evidence suggests that  
63 variations in precipitation patterns influenced the timing and magnitude of this retreat (Moreno et  
64 al., 1999; Rojas et al., 2009). The wintertime climate across South America is strongly influenced  
65 by the southern annular mode (SAM; Hartmann and Lo, 1998), for which its phase and strength is  
66 regulated by changes in the difference of zonal mean sea-level pressure between mid (40°S) and

67 high latitudes (65°S). The SAM in turn modulates the strength and position of the southern  
68 westerly winds (SWW) over decadal to multi-centennial timescales, which exert a large control on  
69 the synoptic scale hydrologic and heat budget (Garreaud et al., 2013). During the LGM and last  
70 deglaciation, paleoclimate data indicates that the position, strength, and extent of the SWW varied  
71 latitudinally, migrating southward during warmer intervals and northward during cooler intervals,  
72 ultimately altering overall ice sheet mass balance (Mercer, 1972; Denton et al., 1999; Lamy et al.,  
73 2010; Kilian and Lamy, 2012; Boex et al., 2013). Terrestrial paleoclimate proxies that indicate  
74 that the CLD was wetter during the LGM and early deglaciation have been used to support the  
75 idea that the SWW migrated northward of 41°S across the CLD (Moreno et al., 1999; Moreno et  
76 al., 2015; Moreno and Videla, 2018; Diaz et al., 2023). Additionally, these proxies indicate a  
77 switch from hyper humid to humid conditions around 17,300 cal yr BP, which was inferred by  
78 Moreno et al. (2015) to indicate the poleward migration of the SWW south of the CLD.

79

80 However, inferring changes in the SWW across the last deglaciation from paleoclimate proxies  
81 can be problematic as outlined by Kohfeld et al. (2013) who compiled an extensive dataset of  
82 paleoclimate archives that record changes in moisture, precipitation-evaporation balance, ice  
83 accumulation, runoff and precipitation, dust deposition, and marine indicators of sea surface  
84 temperature, ocean fronts, and biologic productivity. Kohfeld et al. (2013) conclude that  
85 environmental changes inferred from existing paleoclimate data could be potentially explained by  
86 a range of plausible scenarios for the state and change of the SWW during the LGM and last  
87 deglaciation, such as a strengthening, poleward or equatorward migration, or no change. Climate  
88 model results from Sime et al. (2013) indicate that the reconstructed changes in moisture from  
89 Kohfeld et al. (2013) can be simulated well without invoking large shifts or changes in strength to  
90 the SWW. This discrepancy also exists amongst climate models which diverge on whether the  
91 LGM SWW was shifted equatorward or poleward, and was stronger or weaker than present day  
92 (Togweiler et al., 2006; Menviel et al., 2008; Rojas et al., 2009; Rojas et al., 2013; Sime et al.,  
93 2013; Jiang et al., 2020). Therefore, from paleoclimate proxies and climate models, we still do  
94 not have a firm understanding of how the SWW may have changed during the last deglaciation,  
95 and how these variations may have influenced the deglaciation of the PIS.

96

97 Early paleo ice sheet modelling experiments across the PIS have focused on evaluating the  
98 relationship between the simulated LGM ice sheet geometry in response to spatially uniform  
99 temperature change (Hulton et al., 2002; Sugden et al., 2002; Hubbard et al., 2005). While these  
100 early simulations provided constraints on PIS areal extent, ice volume, and sensitivity to LGM  
101 temperature depressions, spatially varying temperature and precipitation were not considered.  
102 Recently, Yan et al. (2022) simulated the PIS behavior at the LGM using an ensemble of climate  
103 model output from the Paleoclimate Modelling Intercomparison Project (PMIP4; Kageyama et al.,  
104 2021). Results best matching the empirical reconstructions from PATICE (Davies et al., 2020)  
105 suggest that reduction in temperature was likely the main driver of PIS LGM extent, although the  
106 authors found that variation in regional LGM precipitation anomaly can have large impacts on the  
107 simulated ice sheet geometry. This evidence is supported by recent glacier modelling across the  
108 northeastern Patagonian Andes which suggests that increases in precipitation during the  
109 termination of the LGM are necessary to achieve modeled fit with reconstructed glacier extent  
110 (Muir et al., 2023; Leger et al., 2021b). Additionally, Martin et al. (2022) found that precipitation  
111 greater than present day is needed to explain late glacial and Holocene ice readvance of the Monte  
112 San Lorenzo ice cap, lying to the southeast of the current Northern Patagonian Ice Field. These

113 regional studies therefore provide further evidence that late glacial and deglacial variability in  
114 precipitation, perhaps driven by changes in the SWW, influenced PIS retreat and readvance over  
115 numerous timescales.

116  
117 To advance our understanding of the last glacial and deglacial ice behavior across the CLD, we  
118 use a numerical ice sheet model to simulate the LGM ice geometry and deglacial ice retreat using  
119 transiently evolving boundary conditions from a climate model simulation of the last 21,000 years  
120 (TraCE-21ka; Liu et al., 2009; He et al., 2013) which simulates large scale variability in the  
121 strength and position of the SWW (Jiang and Yan, 2020). Because there is a lack of transiently  
122 evolving ice sheet model simulations of the PIS across the last deglaciation, our aim is to provide  
123 possible constraints on the nature of ice retreat across the CLD region, from which the  
124 reconstructions (PATICE; Davies et al., 2020) are uncertain. Also, by assessing the sensitivity of  
125 our ice sheet experiments to a range of climatic boundary conditions, we aim to provide additional  
126 insight into the dominant climatic controls on the deglacial evolution of the PIS in the CLD region.

127

## 128 **2 Methods: Model description and setup**

129

### 130 **2.1 Ice sheet model**

131

132 In order to simulate the ice margin migration across the CLD during the LGM and last deglaciation,  
133 we use the Ice Sheet and Sea-level System Model (ISSM), a thermomechanical finite-element ice  
134 sheet model (Larour et al., 2012). Because of the high topographic relief across the CLD and  
135 associated impact on ice flow, we use a higher-order approximation to solve the momentum  
136 balance equations (Dias dos Santos et al., 2022). This ice flow approximation is a depth-integrated  
137 formulation of the higher-order approximation of Blatter (1995) and Pattyn (2003), which allows  
138 for an improved representation of ice flow compared with more traditional approaches in paleo-  
139 ice flow modelling (e.g., Shallow Ice Approximation or hybrid approaches; Hubbard et al., 2005;  
140 Leger et al., 2021b; Yan et al., 2022), while allowing for reasonable computational efficiency. Our  
141 model domain comprises the northernmost LGM extent of the PIS across the CLD, extending  
142 beyond the LGM ice extent reconstructed from Davies et al. (2020) and ends along the northern  
143 shore of the Golfo de Ancud (Figure 2).

144

145 We rely on anisotropic mesh adaptation to create a non-uniform model mesh that varies based  
146 upon gradients in bedrock topography from the General Bathymetric Chart of the Oceans  
147 (GEBCO; GEBCO Bathymetric Compilation Group, 2021), a terrain model for ocean and land.  
148 For the land component, the GEBCO model uses version 2.2 of the Surface Radar Topography  
149 Mission data (SRTM15\_plus; Tozer et al., 2019), to create a 15 arc second gridded output of terrain  
150 elevation relative to sea level. Our ice sheet model horizontal mesh resolution varies from 3 km  
151 in areas of low bedrock relief to 450 meters in areas where gradients in the bedrock topography is  
152 high and comprises 40,000 model elements. We impose no boundary conditions of ice flow and  
153 thickness at the southern extent of our model domain. Due to the north-south nature of the  
154 simulated ice divide during the last deglaciation (see Figure 4), inflow from the south and into our  
155 model domain is minimal and was found to not impact our results.

156

157

158

159  
160  
161  
162  
163  
164  
165  
166  
167  
168  
169  
170  
171  
172  
173  
174  
175  
176  
177  
178  
179  
180  
181  
182  
183  
184  
185  
186  
187  
188  
189

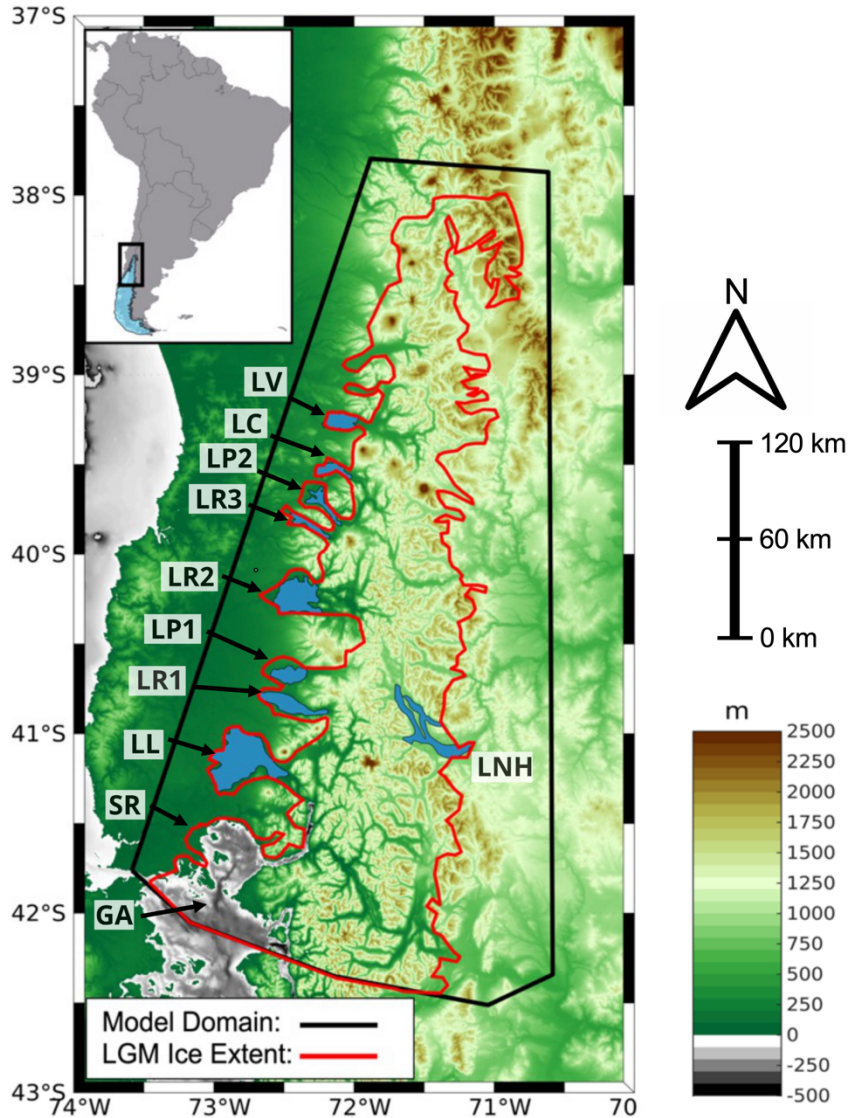


Figure 2. Bedrock topography for our study area (meters). Our model domain (shown as the black line), encompasses the reconstructed LGM ice limit (shown in red) from PATICE (Davies et al., 2020). Present day lakes are shown in blue, with abbreviated names as: SR (Seno de Reloncaví), GA (Golfo de Ancud), LL (Lago Llanquihue), LR1 (Lago Rupanco), LP1 (Lago Puyehue), LR2 (Lago Ranco), LR3 (Lago Riñihue), LP2 (Lago Panguipulli), LC (Lago Calafquén), LV (Lago Villarica), LNH (Lago Nahuel Huapi).

190  
191  
192  
193  
194  
195  
196  
197

Although geomorphological evidence suggests that while southernmost glaciers across the PIS may have been temperate with warm based conditions during the LGM, there may have been periods where ice lobes were polythermal (Darvill et al., 2016). However, recent ice flow modelling (Leger et al., 2021b) suggests that varying ice viscosity mainly impacts the accumulation zone thickness in simulations of paleoglaciers in Northeastern Patagonia, with minimal impacts on overall glacier length and extent. Accordingly, based on sensitivity tests (see supplement section S1), our model is 2-dimensional and we do not solve for ice temperature and viscosity allowing for increased computational efficiency. For our purposes, we use Glen’s flow

198 law (Glen, 1955) and set the ice viscosity following the rate factors in Cuffey and Paterson (2010)  
199 assuming an ice temperature of  $-0.2^{\circ}\text{C}$ . We use a linear friction law (Budd et al., 1979)

$$200 \tau_b = -k^2 N u_b \quad (1)$$

201 where  $\tau_b$  represents the basal stress,  $N$  represents the effective pressure, and  $u_b$  is the magnitude  
202 of the basal velocity. Here  $N = g(\rho_i H + \rho_w Z_b)$ , where  $g$  is gravity,  $H$  is ice thickness,  $\rho_i$  is the  
203 density of ice,  $\rho_w$  is the density of water, and  $Z_b$  is bedrock elevation following Cuffey and Paterson  
204 (2010).

205 The spatially varying friction coefficient,  $k$ , is constructed following Åkesson et al. (2018):

$$206 k = 200 \times \frac{\min[\max(0, z_b + 600), z_b]}{\max(z_b)} \quad (2)$$

207 where  $z_b$  is the height of the bedrock with respect to sea level. Using this parameterization, basal  
208 friction is larger across high topographic relief and lower across valleys, and areas below sea level.

209 To account for the influence of glacial isostatic adjustment (GIA), we prescribe a transiently  
210 evolving reconstruction of relative sea level from the global GIA model of the last glacial cycle  
211 from Caron et al. (2018). This includes three physical components: 1) Bedrock vertical motion  
212 2.) Eustatic sea level, and 3.) Geoid changes. The time series we use to prescribe GIA is from the  
213 model average of an ensemble of GIA forward model estimations from Caron et al., 2018. The  
214 prescribed GIA is in good agreement (Figure S2) with a reconstruction of relative sea-level change  
215 from an isolation basin in central Patagonia (Troch et al., 2022). This methodology has been  
216 applied in recent modelling following Cuzzzone et al. (2019) and Briner et al. (2020).

## 222 2.2 Experimental Design

223 In order to simulate the ice history at the LGM and across the last deglaciation we use climate  
224 model output from the National Center for Atmospheric Research Community Climate System  
225 Model (CCSM3) TraCE-21ka transient climate simulation of the last deglaciation (Liu et al., 2009;  
226 He et al., 2013). Monthly mean output of temperature and precipitation are used from these  
227 simulations as inputs to our glaciological model (full climate forcings details are further described  
228 in section 2.4) and we use the monthly mean output every 50 years across the last deglaciation.  
229 Large, multi-proxy reconstructions from He and Clark (2022), Liu et al. (2009), He et al. (2011),  
230 and Shakun et al. (2012; 2015) have all demonstrated good agreement between TRACE 21k and  
231 a wide variety of paleo-proxy data during the last deglaciation that include records from the West  
232 Antarctic and South America.

## 234 2.3 Surface Mass Balance

235 In order to simulate the deglaciation of the PIS across our model domain we require inputs of  
236 temperature and precipitation to estimate the surface mass balance. To derive snow and ice melt  
237 we use a positive degree day model (Tarasov and Peltier, 1999; Le Morzadec et al., 2015; Cuzzzone  
238 et al., 2019; Briner et al., 2020). Our degree day factor for snow melt is  $3 \text{ mm } ^{\circ}\text{C}^{-1}\text{day}^{-1}$  and  $6 \text{ mm } ^{\circ}\text{C}^{-1}\text{day}^{-1}$   
239 for bare ice melt, and we use a lapse rate of  $6 \text{ } ^{\circ}\text{C}/\text{km}$  to adjust the temperature of the  
240

241 climate forcings to surface elevation, which are within a range of typical values used to model  
 242 contemporary and paleo glaciers across Patagonia (see Fernandez et al., 2016 Table 3; Yan et al.,  
 243 2022). The hourly temperatures are assumed to have a normal distribution, of standard  
 244 deviation 3.5 degrees Celsius around the monthly mean. An elevation-dependent desertification  
 245 is included (Budd and Smith, 1981) which reduces precipitation by a factor of 2 for every kilometer  
 246 change in ice sheet surface elevation. We note that the values in the surface mass balance  
 247 parameters were chosen to provide a reasonable fit within 5% between the simulated LGM ice  
 248 sheet area and the reconstructed ice area from PATICE (see Figure 4 and 10).

249  
 250 **2.4 Climate forcings**  
 251

252 In order to scale monthly temperature and precipitation across the LGM and last deglaciation we  
 253 applied a commonly used modeling approach (Pollard et al., 2012; Seguinot et al., 2016; Golledge  
 254 et al., 2017; Tigchlaar et al., 2019; Clark et al., 2020; Briner et al., 2020; Cuzzone et al., 2022; Yan

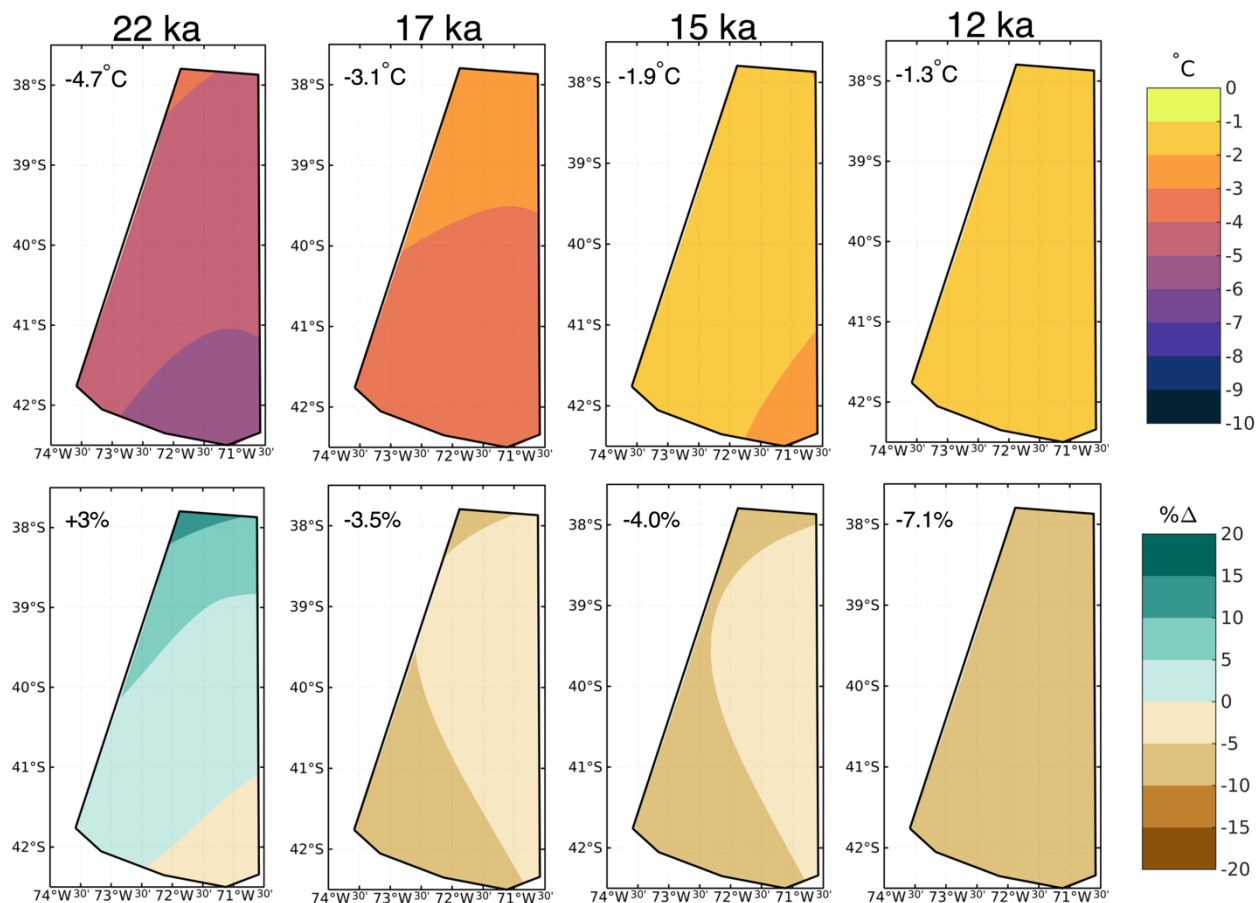


Figure 3. The bilinearly summer (DJF) temperature (top row) and winter (JJA) precipitation anomalies (bottom row) from TraCE-21ka at 22 ka, 17 ka, 16 ka, and 12 ka. Anomalies are taken as the difference between the corresponding time period and preindustrial (LGM-PI), with the precipitation anomalies expressed as the percent difference from preindustrial. The area averaged value of the anomaly is shown in the upper left corner of each

255  
 256 et al., 2022; equations 3 and 4). First, we use the monthly mean climatology of temperature and  
 257 precipitation for the period 1979-2018 ( $\bar{T}_{(1979-2018)}$ ,  $\bar{P}_{(1979-2018)}$ ) from the Center for Climate

258 Resilience Research Meteorological dataset version 2.0 (CR2MET; Boisier et al., 2018). This  
 259 output, which uses information from a climate reanalysis and is calibrated against rain-gauge  
 260 observations, is provided at 5 km spatial resolution.

261  
 262 We then bilinearly interpolate these fields onto our model mesh.

$$263 \quad T_t = \bar{T}_{(1979-2018)} + \Delta T_t \quad (3)$$

$$264 \quad P_t = \bar{P}_{(1979-2018)} + \Delta P_t \quad (4)$$

265  
 266  
 267 Next, anomalies of the monthly temperature and precipitation fields from TraCE-21ka (Liu et al.,  
 268 2009; He et al., 2013) are computed as the difference from the preindustrial control run and  
 269 interpolated onto our model mesh ( $\Delta T_t$  and  $\Delta P_t$ ). These anomalies are added to the contemporary  
 270 monthly mean as shown in equations 3 and 4, to produce the monthly temperature and precipitation  
 271 fields at LGM and across the last deglaciation ( $T_t$  and  $P_t$ ). In Figure 3 anomalies from preindustrial  
 272 of summer temperature and winter precipitation are shown for 22 ka, 17 ka, 15 ka, and 12 ka.  
 273  
 274

## 275 **2.5 Ice front migration and iceberg calving**

276  
 277 We simulate calving where the PIS interacts with ocean, but do not include any treatment of  
 278 calving in proglacial lakes (see section 4.3). We track the motion of the ice front using the level-  
 279 set method described in Bondzio et al. (2016; equation 3) in which the ice velocity  $v_f$ , is a function  
 280 of the ice velocity vector at the ice front ( $v$ ), the calving rate ( $c$ ), the melting rate at the calving  
 281 front ( $\dot{M}$ ), and where  $n$  is the unit normal vector pointing horizontally outward from the calving  
 282 front. For these simulations the melting rate is assumed to be negligible compared to the calving  
 283 rate, so  $\dot{M}$  is set to 0.

$$284 \quad v_f = v - (c + \dot{M}) n \quad (5)$$

285  
 286 To simulate calving we employ the more physically based Von Mises stress calving approach  
 287 (Morlighem et al., 2016) which relates the calving rate ( $c$ ) to the tensile stresses simulated within  
 288 the ice, where  $\tilde{\sigma}$  is the von Mises tensile strength,  $\|v\|$  is the magnitude of the horizontal ice  
 289 velocity, and  $\sigma_{max}$  is the maximum stress threshold which has separate values for tidewater and  
 290 floating ice, namely 1 MPa and 200 kPa.  
 291  
 292

$$293 \quad c = \|v\| \frac{\tilde{\sigma}}{\sigma_{max}} \quad (6)$$

294  
 295 The ice front will retreat if von Mises tensile strength exceeds the user defined stress threshold.  
 296 This calving law has been applied in Greenland to assess marine terminating icefront stability  
 297 (Bondzio et al., 2016; Morlighem et al., 2016; Choi et al., 2021; Cuzzone et al., 2022) and for our  
 298 simulations applies where ocean is present such as the Seno de Reloncaví and the Golfo de Ancud  
 299 (see Figure 2).

## 300 **3 Results**

301  
 302



### 3.1 Simulated LGM state

In order to arrive at a steady state LGM ice geometry, we first initialize our model with an ice-free configuration. A constant LGM monthly climatology of temperature and precipitation are then applied, as well as the prescribed GIA from Caron et al. (2018). We allow the ice sheet to relax for 10,000 years, during which, the ice sheet is free to grow and expand until it reaches a steady state ice geometry and volume, in equilibrium with the climate forcings.

At 22 ka, Trace-21ka simulates an area averaged summertime (DJF) cooling of 4.7°C relative to the PI across our model domain (Figure 3). The LGM cooling increases from north to south, with the greatest magnitude of cooling occurring across the southern portion of our model domain of up to 6°C. During winter (JJA), Trace-21ka simulates an overall wetter climate across our model domain during the LGM relative to the PI. While the area-averaged LGM precipitation anomaly is small (3% higher), the LGM precipitation anomaly increases from south to north, with Trace-21ka simulating 10-15% more wintertime precipitation during the LGM than the PI across the northern portion of the model domain.

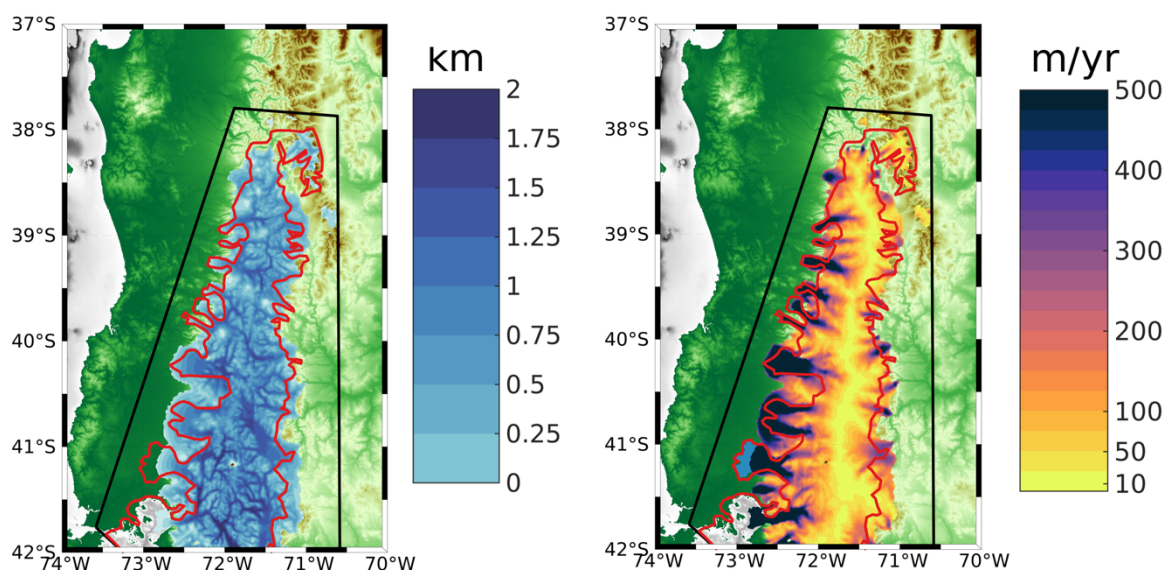


Figure 4. The simulated LGM ice thickness (km; left panel) and the simulated LGM ice surface velocity (m/yr; right panel) is shown. The black outline denotes our ice sheet model boundary, and the red line denotes the LGM reconstructed ice extent from PATICE (Davies et al., 2020).

Bedrock elevation increases from west to east, with deep valleys interspersed across most of our model domain (Figure 2). LGM ice thickness is greatest in these valleys (upwards of 2000 meters) where driving stresses dominate and where bedrock geometry controls the flow of ice from higher terrain and through these valleys (Figure 4). Across the highest terrain such as the many volcanoes across the CLD, ice is comparatively thinner than the surrounding valleys. An ice divide is present as slow ice velocities in the interior of the ice sheet, which give way to fast flowing outlet glaciers especially on the western margin of the CLD where velocities reach in excess of 500 m/yr and in some location up to 2 km/yr. The simulated LGM ice sheet area across the CLD is 414,120 km<sup>2</sup>,

328 which is within 1% of the area calculated from the PATICE reconstruction (414,690 km<sup>2</sup>; Figure  
329 10). This agreement is in part due to the tuning of our degree day factors as discussed in section  
330 2.3, and gives confidence to our ability to simulate a reasonable LGM ice sheet across the CLD  
331 and throughout the last deglaciation.

332

### 333 3.2 Simulation of the Last Deglaciation

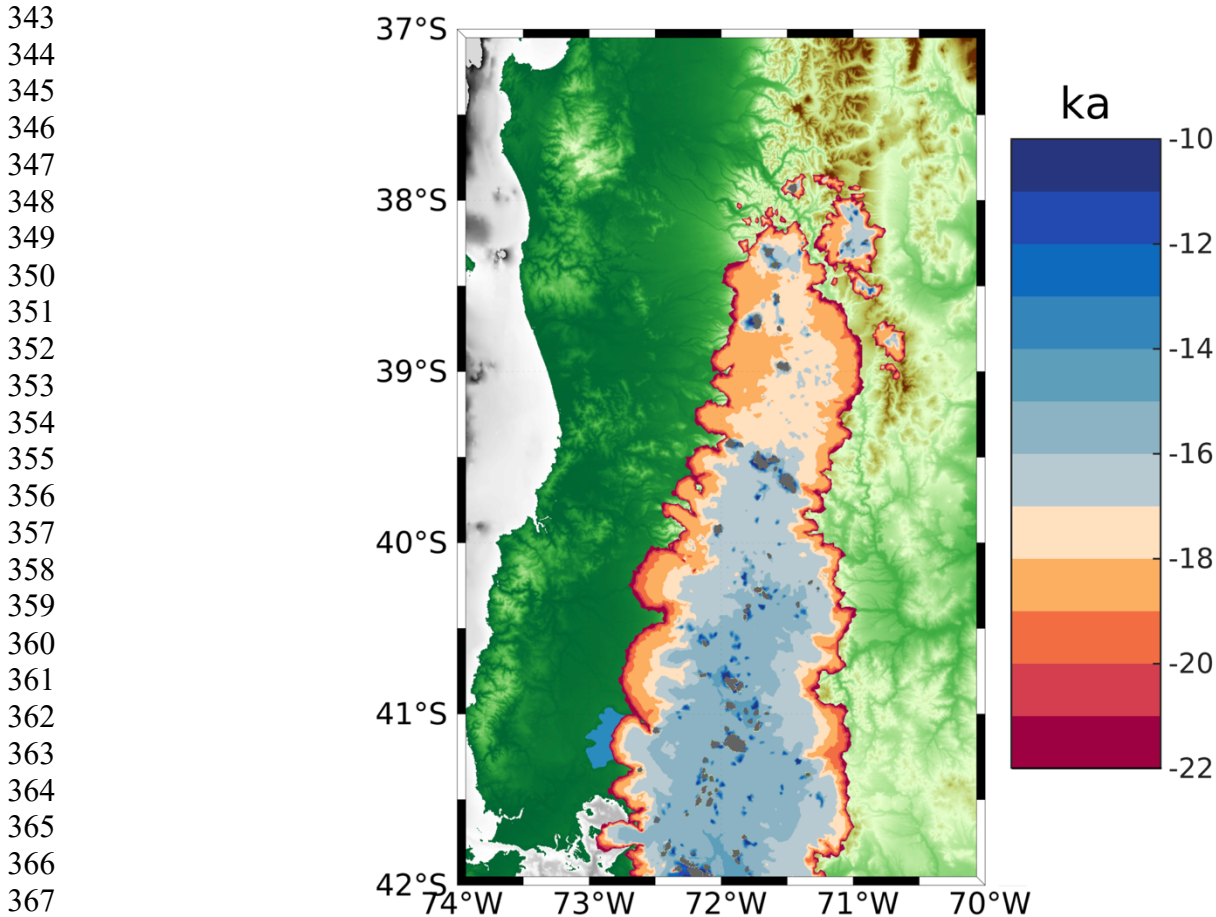
334

335 Monthly mean temperature and precipitation, taken every 50 years from the TraCE-21ka (Liu et  
336 al., 2009; He et al., 2013) experiment is used to drive our simulation of ice history across the last  
337 deglaciation (22 ka – 10 ka). The transient simulation is initialized with the LGM ice sheet  
338 geometry shown in Figure 4, and is run forward with the appropriate climate boundary conditions  
339 until 10 ka.

340

#### 341 3.2.1 Pattern of Deglaciation

342



369 Figure 5. The simulated deglaciation age for the transient simulation from the LGM to 10 ka. The gray color  
370 indicates where ice persists after 10 ka.

371 From the resulting transient simulation, we calculate the timing of deglaciation across our model  
372 domain (Figure 5) as the youngest age at which grid points become ice free. Our map of the

373 simulated deglaciation can be paired with a timeseries of the rate of ice mass change (Figure 6) to  
374 highlight some key features in the magnitude and timing of ice retreat between 22 ka and 10 ka.

375  
376 Between 22 ka to 19 ka, the ice sheet undergoes periods of minor to moderate ice mass loss and  
377 gain in an interval of time where summer temperature anomalies (Figure 6) and the corresponding  
378 ice margin remain relatively stable (Figure 5). Between 19 ka and 18.5 ka, coincident with a rise  
379 in summertime temperature (Figure 6), a pulse of ice mass loss exceeding 5,000 GT/century occurs  
380 before trending toward minimal ice mass loss around 18 ka as the rise in summer temperature  
381 levels off. During this time interval, the ice margin pulls back considerably towards higher terrain  
382 across the northern portion of the model domain (Figure 5), and many of the fast-flowing outlet  
383 glaciers on the western margin retreat back towards the ice sheet interior. Between 18 ka to 16.2  
384 ka, summer temperature rises steadily  $\sim 1.2^\circ\text{C}$  and is punctuated with an abrupt warming of  $\sim 0.5^\circ\text{C}$   
385 at 16 ka (Figure 6). During this interval, ice mass loss remains high and steady at  $\sim 1000$   
386 GT/century with pulses of increased mass loss at 17.8 ka, 16.8 ka, and 16 ka varying between  
387 2000-5000 GT/century (Figure 6).  
388

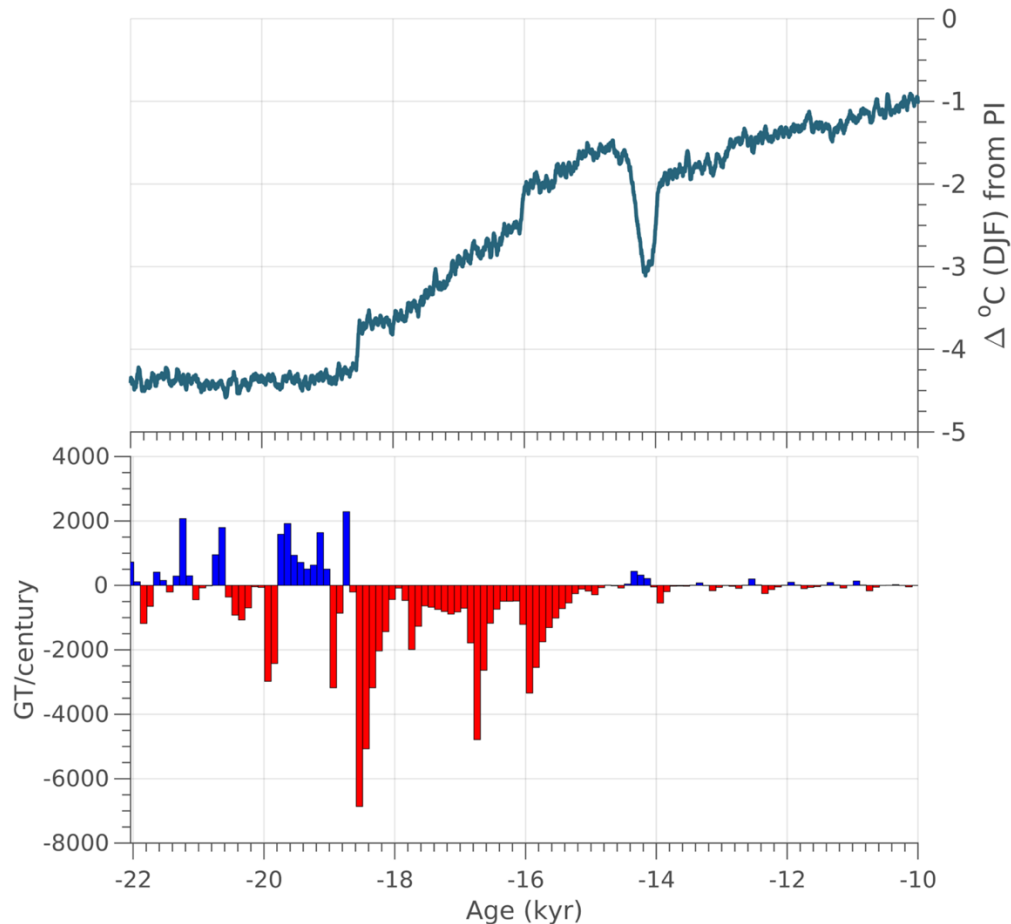


Figure 6. Top Panel: The TraCE-21ka Summer (DJF) temperature anomaly taken as the difference from the preindustrial period, area averaged across our model domain. Bottom Panel: The simulated ice mass change calculated in GT/century across the last deglaciation (22 ka to 10 ka). Red indicates ice mass loss, and blue indicates ice mass gain.

389

390 By 17 ka, the northern portion of the model domain (north of 39.5°S), has generally become ice  
 391 free for the exception of the highest terrain (e.g., mountain glaciers). By 16 ka, between 39.5°S  
 392 and 40.5°S, ice remains only on the highest terrain (Figure 5), however ice cover persists south of  
 393 40.5°S. Between 16 ka and 15 ka, summer temperature rises ~0.5°C (Figure 6) and the remaining  
 394 ice sheet retreats south of 40.5°S. By 15 ka, there is no evidence of an ice sheet, with only  
 395 mountain glaciers and small ice caps (e.g., Cerro Tronador) existing across the high terrain  
 396 throughout the model domain (Figure 5).

397  
 398 After 15 ka, TraCE-21ka simulates a short and abrupt Antarctic Cold Reversal (ACR) between  
 399 14.6 ka and 14 ka (Figure 6), before temperatures continue to rise into the early Holocene. There  
 400 is only a minor ice mass gain (e.g., <500 GT/yr) during the ACR, and minimal fluctuation in ice  
 401 mass after 14 ka. By 10 ka, only small mountain glaciers persist across the high terrain and  
 402 volcanoes of the CLD (gray color in Figure 5).

403  
 404 **3.2.2 Sensitivity Tests**

405  
 406 To better assess how changes in precipitation may modulate the deglaciation across the CLD we  
 407 perform additional sensitivity tests. We refer to the simulation discussed above as our *main*  
 408 *simulation*, where the climate boundary conditions of temperature and precipitation varied  
 409 temporally and spatially across the last deglaciation. Three more simulations are performed where  
 410 temperature is allowed to vary across the last deglaciation, but precipitation remains fixed at a  
 411 given magnitude for a particular time interval. Each experiment is listed below as:

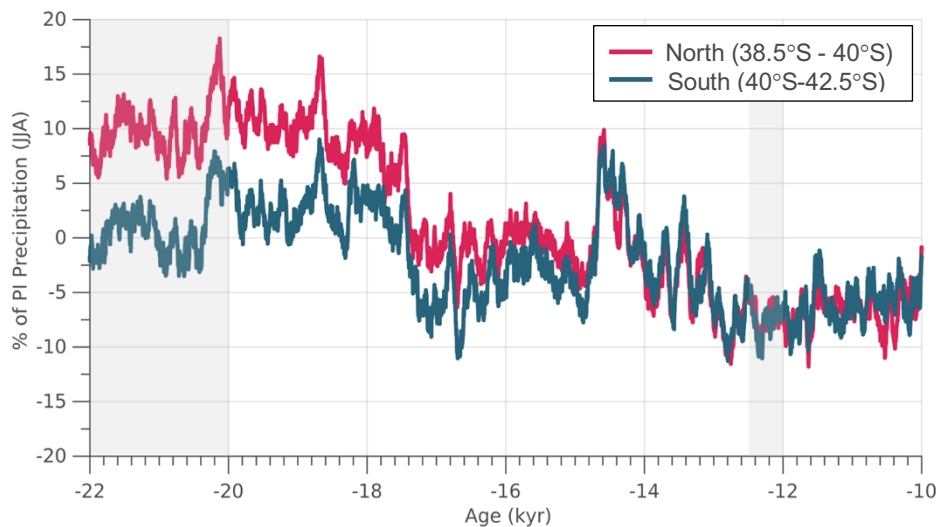


Figure 7. The winter (JJA) precipitation anomaly expressed as the percent difference from the preindustrial period. The area averaged anomaly is shown for the region north of 40°S and for the region south of 40°S (see Figure 2 for reference to the latitudinal range of our model domain). Intervals of time used in the sensitivity tests are highlighted by the gray shading.

412 *Precip. PI:* Monthly precipitation is held constant at the preindustrial mean. Preindustrial  
 413 precipitation is reduced compared to the period 22 ka to 18 ka, but is similar to and higher than  
 414 what is simulated after 18 ka for the exception of the ACR at 14.5 ka (Figure 7).

415 *Precip. 12 ka*: Monthly precipitation is held constant at the 12.5 ka-12 ka mean. This is a  
416 period of reduced precipitation relative to the preindustrial (~7% reduction; Figure 7).

417 *Precip LGM*: Monthly precipitation is held constant to the 22-20 ka mean, which is  
418 approximately 10% higher than preindustrial values across the Northern portion of the model  
419 domain (North of 40°S).

420 Across our model domain during experiment *Precip. PI* (Figure 8A), wintertime precipitation  
421 during the preindustrial is reduced compared to the early deglaciation (22 ka to 18ka) and is similar  
422 to slightly higher particularly south of 40°S after 18 ka (Figure 7). When holding precipitation  
423 constant at the preindustrial mean through the last deglaciation, the ice retreats faster across most  
424 portions of the model domain, particularly along the ice margins and in area north of 40°S. In the  
425 southern portion of our model domain (south of 40°S), where the changes in deglacial precipitation  
426 relative to the preindustrial are lower (Figure 3 and 7), the difference in simulated deglaciation age  
427 are also smaller. In general, the pace of deglaciation increases by up to 1 kyr compared to the  
428 main simulation, with many locations experiencing deglaciation 200-600 yrs earlier than the main  
429 simulation.

430

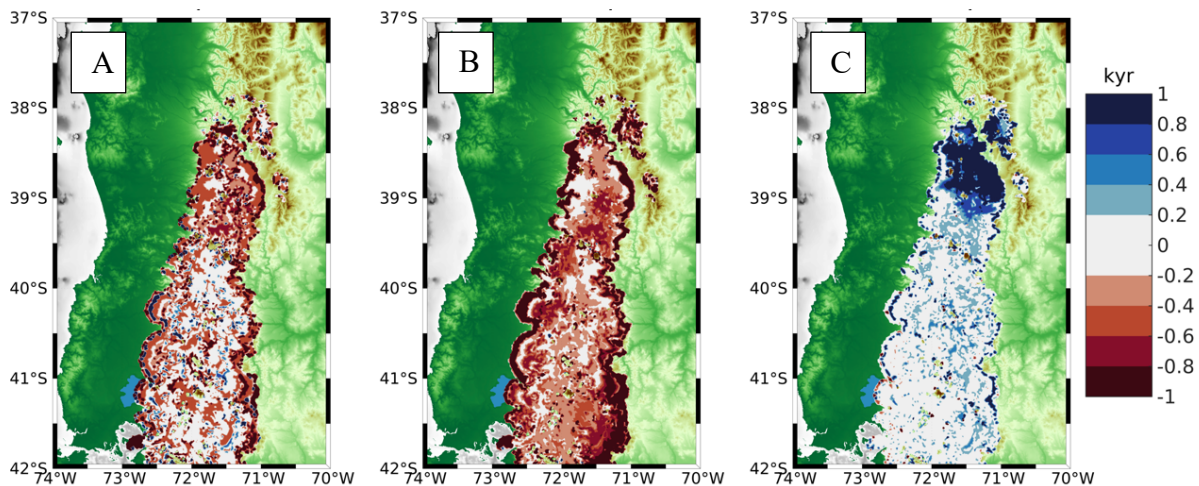


Figure 8. A) The difference in the simulated deglaciation age between sensitivity experiment *Precip. PI*: B.) experiment *Precip. 12 ka* , C.) and experiment *Precip LGM* , from the main simulation. Blue colors indicate slower ice retreat for the sensitivity experiments compared to the main simulation, while red colors indicate faster ice retreat for the sensitivity experiments compared to the main run.

431 For experiment *Precip. 12 ka*, winter precipitation is reduced by up to 7% (Figure 8B) relative to  
432 the preindustrial across the model domain (Figure 3 and 7). In this experiment ice retreats faster  
433 across most of the CLD, from the ice margins and through the interior. Deglaciation along the  
434 margins occurs >1 kyr faster in many locations, and between 200 yrs to 1 kyr faster across portions  
435 of the ice interior. For experiment *Precip LGM*, winter precipitation is increased by up to 10%  
436 (Figure 8C; *Precip LGM*;) across the northern portion of the model domain (north of 40°S) relative  
437 to preindustrial, but is similar to preindustrial values across the southern portion of our model  
438 domain (south of 40°S). In this experiment, with the imposed higher precipitation across the

439 northern portion of the model domain, ice retreats slower during the last deglaciation relative to  
440 our standard simulation by >1 kyr, and in some locations up to 2 kyr.

### 441 3.3 Comparison to the reconstructed deglacial ice extent

442  
443 Shown in Figure 1, PATICE assigns high to medium confidence to the reconstructed LGM (25 ka  
444 – 20 ka) ice extent along most of the western ice margin and portions of the eastern margin, with  
445 low confidence assigned to the northernmost ice extent. The majority of the ice history is poorly  
446 constrained (low confidence) during the deglaciation, and PATICE reconstructs a small cap that

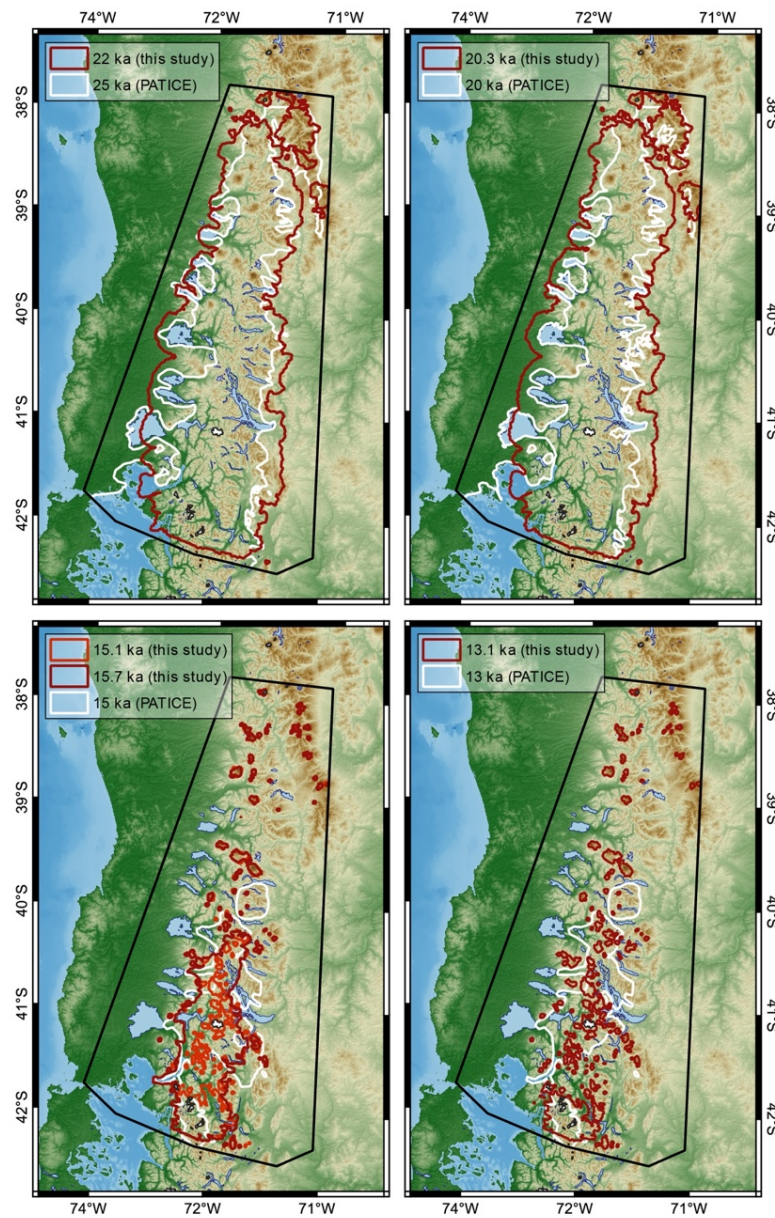


Figure 9. Comparison between the simulated ice extent at time intervals closest to the corresponding reconstructed ice extent from PATICE (Davies et al., 2020).

447 persists across the southern CLD until 10 ka, after which the ice disappears and only the Cerro  
448 Tronador glacier remains (see Figure 13 from Davies et al., 2020). We show the simulated and  
449 reconstructed ice extent in Figure 9 as well as the calculated ice area from PATICE at 20 ka, 15  
450 ka, 13 ka, and 10ka and for our transient simulation in Figure 10. At 22 ka (Figure 9), our model  
451 simulates a generally greater ice extent along the eastern and western margin, except at the Seno  
452 de Reloncaví, Golfo de Ancud, and Lago Llanquihue, where the simulated ice margin does not  
453 advance to the well dated terminal LGM moraines (Mercer, 1972; Porter, 1981; Andersen et al.,  
454 1999; Denton et al., 1999). At 20 ka, the simulated ice area is  $4.1 \times 10^4 \text{ km}^2$  which is nearly identical  
455 to the PATICE areal extent across our model domain (Figure 10). The ice margin at the Seno de  
456 Reloncaví, Lago Llanquihue, and other locations along the eastern boundary in the CLD advances  
457 slightly at 20 ka, but still remain inboard of the PATICE reconstruction for these regions.  
458

459 Between 18.3 ka and 15 ka large scale ice retreat occurs, and the simulated ice sheet loses 90% of  
460 its ice area, while the PATICE reconstruction suggests a reduction of 75% (Figure 10). At 15 ka,  
461 PATICE reconstructs an existing ice cap that separates from the remainder of the PIS to the south  
462 (Figure 9). This is in contrast to the simulated ice extent, which shows that by 15 ka, the PIS  
463 across our model domain has completely retreated and only mountain glaciers or small ice caps  
464 exist amongst the high terrain. However, if we compare the PATICE area at 15 ka and the  
465 simulated ice area at 15.7 ka (Figure 10; green rectangle), they are nearly identical at  $1.2 \times 10^4 \text{ km}^2$ .  
466 While the PATICE ice extent at 15 ka and the simulated ice extent 15.7 ka do not match  
467 completely, the simulated ice extent at 15.7 ka still has evidence of a large ice cap similar to the  
468 PATICE reconstruction. Therefore, the simulated transition from ice sheet to ice cap and to  
469 discrete mountain glaciers occurs between 15.7 ka and 15 ka in our simulations. By 13 ka, our  
470 simulated ice area is 60% lower than the PATICE reconstructed area. By 10 ka this difference is  
471 50%, however by this time the majority of the ice sheet has deglaciated (Figure 10), with our model  
472 simulating discrete mountain glaciers while PATICE reconstructs a small and narrow ice cap  
473 across the high terrain in the southern CLD (also see Figure 1).  
474  
475

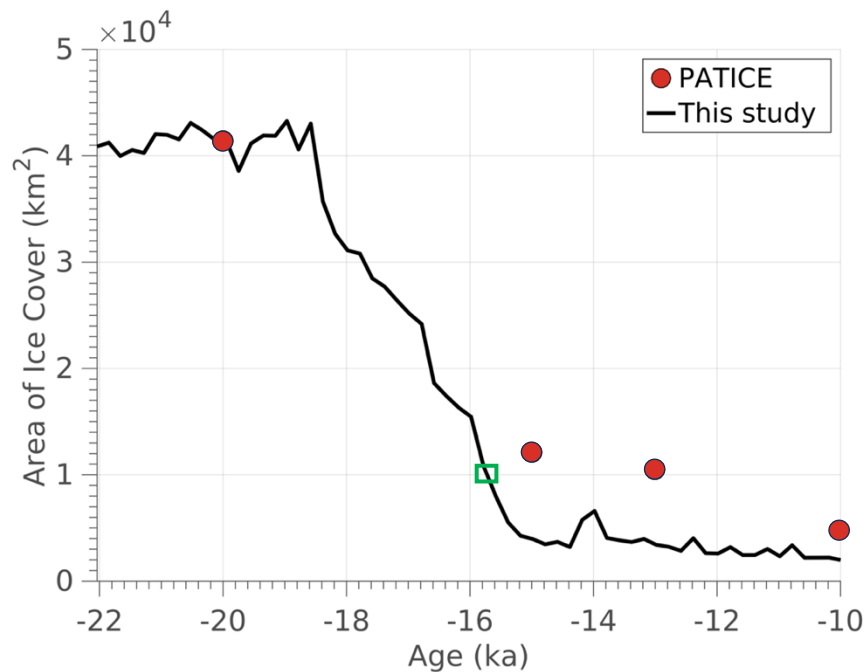


Figure 10. The simulated ice area (km<sup>2</sup>) from 22 ka to 10 ka shown as the black line. The red dots indicate the calculated ice area across our model domain for the reconstructed ice extent from PATICE (Davies et al., 2020). The green rectangle highlights the simulated ice area at 15.7 ka.

477

## 478 4 Discussion

479

### 480 4.1 Climate-ice sensitivity

481

482 Determining the influence of the SWW on the heat and hydrologic budget across South America  
 483 during the LGM and last deglaciation remains difficult, as paleo-proxy data is limited and climate  
 484 models tend to disagree on the evolution of the SWW (Kohfeld, 2013; Berman et al., 2018). And  
 485 while paleo-proxy evidence does suggest wetter conditions across the CLD during the late glacial  
 486 (Moreno and Videla, 2018), linking this variability to changes in the position and strength of the  
 487 SWW remains difficult (Kohfeld et al., 2013).

488

489 The scale at which we deduce ice history and climate interactions is also important. Looking at  
 490 the PIS as a whole, recent numerical ice sheet modelling studies indicate that the simulated ice  
 491 extent and volume for the entire PIS at the LGM is largely controlled by the magnitude of the  
 492 temperature anomaly compared to present day (Yan et al., 2022). However, regional scale ice  
 493 flow modelling informed by geologic constraints on past ice margin extent show that higher  
 494 precipitation during the LGM (Leger et al., 2021b), the late glacial, and the Holocene (Muir et al.,  
 495 2023; Martin et al., 2022) is needed to support model-data agreement. It appears that during the  
 496 LGM a northward shift in the SWW (Kohfeld et al., 2013; Rojas et al., 2009; Togweillier et al.,  
 497 2006) or a strengthening or expansion of the wind belt (Lamy et al., 2010) is perhaps the most  
 498 likely scenario, with high frequency variability possible during the deglaciation as atmospheric  
 499 reorganization altered the heat and hydrologic budget as recorded by glacier and ice sheet change  
 500 (Davies et al., 2020; Boex et al., 2013).



501 We analyzed outputs of the wintertime (JJA) 925 hPa zonal wind as the mean over 500 yr periods  
502 from TraCE-21ka for the LGM (22-21ka), 18ka (18.5-18ka), 16ka (16.5-16ka), 14ka (14.5-14ka),  
503 12ka (12.5-12ka) and the Preindustrial (Supplemental section 3, Figures S3 A-E). Across our  
504 model domain and to its south, relative to the PI, zonal winds are stronger during the LGM with a  
505 southerly displacement (Figure S3A first and second column). During 18ka (Figure S3B), the zonal  
506 wind increases in strength relative to the PI, with the stronger winds having wider latitudinal  
507 coverage, particularly across our model domain. While the mean position of the SWW is poleward  
508 at 18ka relative to the PI (Jiang and Yan, 2022), across Patagonia the simulated position of the  
509 maximum zonal wind is at the same latitudinal band as the PI. At 16ka, the zonal wind is stronger  
510 across our domain and Patagonia (Figure S3C) relative to the PI, although not as large as the  
511 differences during 18ka. By 14ka, the strength in the zonal winds across Patagonia and our model  
512 domain are similar to slightly stronger than the PI (Figure S3D), however, the zonal wind  
513 maximum is situated more equatorward across our model domain relative to the PI. By 12ka  
514 (Figure S3E), the zonal wind is similar to slightly weaker than the PI across our model domain,  
515 although it is stronger relative to the PI to the south of our model domain across central and  
516 southern Patagonia. The position of the maximum zonal winds is also displaced further south  
517 relative to the PI. These changes in strength and position of the simulated SWW during the last  
518 deglaciation are similar to the findings of Jian and Yan (2020), which found that relative to the  
519 Preindustrial (PI), TraCE-21ka simulates a more poleward subtropical and subpolar jet over the  
520 Southern hemisphere at the LGM. During the remainder of the LGM and last deglaciation, the  
521 overall position of the SWW migrates northward in TraCE-21ka, with poleward displacements  
522 during Heinrich Stadial 1 (HS1), equatorward displacements during the Antarctic Cold Reversal  
523 (ACR), and poleward displacements during the Younger Dryas (YD), similar to our analysis.

524  
525 Additionally, we evaluated the wintertime (JJA) low-level (850 hPa) moisture flux convergence  
526 from TraCE-21ka (MFC; Supplement section 4, Figure S4A-E), which is influenced by the mean  
527 flow and transient eddies in the extratropical hydrologic cycle (Peixoto and Oort, 1992). During  
528 the LGM and 18 ka, MFC increases across our model domain, consistent with a convergence of  
529 the mean flow moisture fields relative to the PI (Figure S4 A, B). During the LGM and 18ka, we  
530 note that TraCE-21ka simulates higher JJA precipitation anomalies (relative to the PI) across our  
531 model domain (Figure 7). While our analysis cannot directly constrain the source of the positive  
532 precipitation anomalies (e.g., mean flow, storms), the strength of the simulated SWW in TraCE-  
533 21ka increases across our model domain (Figure S3 A, B) coincident with the increases in MFC,  
534 which may contribute to the positive precipitation anomalies at these time intervals (Figure 7). By  
535 16ka, there is increased divergence in the 925 hPa winds and moisture relative to the PI (Figure  
536 S4 C). Decreased MFC relative to the PI coincides with a reduction in precipitation across our  
537 model domain that is similar to or less than the PI (Figure 7). We note that the ice thickness  
538 boundary conditions used in the TraCE-21ka come from the Ice5G reconstruction (Peltier, 2004),  
539 which has the PIS being completely deglaciated by 16ka. However, our analysis cannot  
540 decompose whether the simulated changes in precipitation and MFC are a consequence of the  
541 coupling between regional atmospheric circulation and the ice thickness boundary conditions used  
542 in TraCE-21ka or if these changes represent wider interactions with changes in hemispheric  
543 atmospheric circulation. By 14ka, and during the ACR, MFC increases relative to the PI (Figure  
544 S4D). This is consistent with a simulated equatorward migration of the SWW as shown in Jiang  
545 and Yan (2020) and our analysis (Figure S3D), and positive anomalies in precipitation across our  
546 model domain relative to the PI (Figure 7). By 12ka, precipitation across our model domain is

547 reduced relative to the PI (Figure 3 and 7), and TraCE-21ka simulates a reduction in the MFC as  
548 well as a poleward migration of the SWW (Figure S3E; Jiang and Yan, 2020).

549  
550 When considering proxy records of precipitation across the CLD, there is reasonable agreement  
551 with the changes in precipitation simulated by TraCE-21ka. Moreno et al. (1999; 2015) and  
552 Moreno and Videla (2018) find that wetter than present day conditions existed across the CLD  
553 during the LGM and early deglaciation which is consistent with the precipitation anomalies  
554 simulated by TraCE-21ka (Figure 3 and 7). These changes in paleoclimate proxies are attributed  
555 to an intensified storm track associated with an equatorward shift of the SWW (Moreno et al. 1999;  
556 2015). While TraCE-21ka instead simulates a poleward shift of the SWW during these time  
557 intervals, increases in precipitation and the intensification of the storm track as inferred by Moreno  
558 et al. (2015) may also be consistent with a strengthening of the SWW as simulated by TraCE-21ka  
559 during these intervals (Figure S3 A, B; Rojas et al., 2009; Sime et al., 2013; Kohfeld et al., 2013).  
560 Moreno et al. (2015) note that rapid warming ensues across the CLD around 17,800 cal yr BP,  
561 which is similar to the timing of deglacial warming as simulated by TraCE-21ka around 18.5 ka  
562 (Figure 6). Coincident with this rapid temperature rise, Moreno et al. (2015) note a shift from  
563 hyper humid to humid conditions which aligns well with decreases in the simulated precipitation  
564 in TraCE-21ka across our model domain (Figure 7). Lastly, Moreno et al. (1999; 2015) find that  
565 colder and wetter conditions occur across the CLD during the ACR, and infer an equatorward  
566 expansion of the SWW as a potential cause. While TraCE-21ka simulates an abrupt and short  
567 ACR, it does simulate an equatorward expansion of the SWW (Figure S4 D; Jian and Yan, 2020),  
568 associated cooling (Figure 6), and increases in precipitation (Figure 7) that agree with the proxy  
569 data.

570  
571 Prior numerical ice flow modelling has indicated that precipitation played an important role in  
572 controlling the extent of paleoglaciers across the PIS (Muir et al., 2023; Leger et al., 2021b) by  
573 modulating the pace and magnitude of ice retreat and advance during deglaciation (Martin et al.,  
574 2022). Much of the TraCE-21ka simulated winter precipitation anomalies shown in Figure 3 and  
575 7 are within 10% of the preindustrial value. The sensitivity tests conducted here suggest that  
576 modest changes (~10%) in precipitation can alter the pace of ice retreat across the CLD on  
577 timescales consistent with the resolution of geochronological proxies constraining past ice retreat.  
578 We note that while TraCE-21ka simulates variations in precipitation across our model domain that  
579 are consistent with hydroclimate proxies discussed above (Moreno et al., 1999; 2015; 2018), the  
580 magnitude of those changes is not as large as proxy data across the CLD indicate. For example,  
581 hydroclimate proxies suggest that the LGM and early deglaciation was up to 2 times wetter across  
582 the CLD than present day (Moreno et al., 1999; Heusser et al., 1999). Therefore, we can deduce  
583 from our sensitivity analysis here that higher precipitation anomalies during the LGM and last  
584 deglaciation, forced by proposed changes in the SWW (Moreno et al., 1999; 2015), may have  
585 helped offset melt from deglacial warming thereby influencing the pacing of early deglacial ice  
586 retreat in this region.

#### 587 588 ***4.2 Ice retreat during the Last Deglaciation***

589  
590 The PATICE dataset (Davies et al., 2020) serves as the best available reconstruction of ice margin  
591 change for the PIS across the last deglaciation. This state-of-the-art compilation provides an  
592 empirical reconstruction of the configuration of the PIS as isochrones every 5 ka, from 35 ka to

593 present, based on detailed geomorphological data and available geochronological evidence.  
594 Because geochronological constraints on past PIS change are limited, particularly in the CLD, the  
595 PATICE reconstruction assigns qualitative confidence to its reconstructed ice margins. Where  
596 there is agreement between geochronological and geomorphological indicators of past ice margin  
597 history (i.e., moraines), high confidence is assigned. Where geomorphological evidence suggests  
598 the existence of past ice margins, but lacks a geochronological constraint, medium confidence is  
599 assigned. Lastly, low confidence is assigned where there is a lack of any indicators of past ice sheet  
600 extent, where the ice limits result in interpolated interpretations from immediately adjacent  
601 moraines from valleys that have been mapped and dated. Across the CLD, the LGM (25 ka, 20 ka)  
602 ice extent is well constrained by geologic proxies particularly in the west and southwest (Figure  
603 1). The moraines that constrain the piedmont ice lobes that formed along the western boundary  
604 have reasonable age control (Denton et al., 1999; Moreno et al., 1999; Lowell et al., 1995), giving  
605 confidence to the LGM ice margin limits. Beyond this region, age control is sparse along the  
606 western boundary for the timing of LGM ice extent, but the existence of well-defined moraines  
607 along lakes in the northern CLD are assumed to be in sync with those moraines deposited to the  
608 south (Denton et al., 1999). However, low confidence remains in the geologic reconstruction of  
609 the LGM ice boundary along the eastern margin where little to no chronological constraints are  
610 available. In general, deglaciation from the maximum LGM ice extent begins between 18 – 19 ka  
611 (Davies et al., 2020), however, poor age control and a lack of geomorphic indicators make it  
612 difficult to constrain the ice extent across this region during the deglaciation. For instance, a single  
613 cosmogenic nuclide surface exposure date retrieved from the Nahuel Huapi moraine yielded an  
614 age of ~31.4 ka (Zech et al., 2017; 41.04° S, 71.15° W). While it is assumed that the ice limit  
615 behaved similarly both to the west and east, the limited existing data prevents a comprehensive  
616 understanding of the ice extent at the northeastern margin. This induces the highest level of  
617 uncertainty in the reconstruction and hinders our data model comparison. Therefore, we rely on  
618 the PATICE dataset interpolated isochrones (low confidence) for this northeastern region as the  
619 state-of-the-art reconstruction.

620  
621 In regards to ice area and extent, our simulated ice sheet at the LGM using TraCE-21ka climate  
622 boundary conditions agrees well with the PATICE reconstruction (Figure 10). Our simulations  
623 reveal that deglaciation began between 19 ka to 18 ka, consistent with the Davies et al. (2020)  
624 reconstruction. Notably, the simulated timing of deglaciation agrees with moraine records further  
625 south on the eastern side, such as in Río Corcovado (~43° S, Leger et al., 2021a; 17.9 ka), Río  
626 Cisnes (~44° S, Garcia et al., 2019; ~19ka), Lago Palena/General Vintter (~44° S, Soteres et al.,  
627 2022; 19.7 ka), and Río Ñirehuao (~45° S, Peltier et al., 2023; ~18.5 ka). On the other hand,  
628 glaciers are thought to have withdrawn from their LGM position later between ~18 - 17 ka on the  
629 northwestern margin (~41° S, Denton et al., 1999; Moreno et al., 2015), in the southern (~46° S,  
630 Kaplan et al., 2004), and southernmost regions (~52° S, McCulloch et al., 2000; 2005; Kaplan et  
631 al., 2008; Peltier et al., 2021). The simulated ice retreat continues until 15 ka, with the largest  
632 pulses in ice mass loss occurring at 18.6 ka, 16.8 ka, and 16 ka (Figure 6). Where PATICE  
633 estimates an ice cap around 15 ka (~40°S), our simulations reveal that glaciation was restricted to  
634 high elevations. After 15 ka, mountain glaciers remain in our simulation but there is no presence  
635 of a large ice cap as reconstructed in PATICE. Comparison between the model simulations and  
636 PATICE becomes difficult during the 15 -13 ka period as confidence in the geologic reconstruction  
637 is low due to a lack of geochronological and geomorphological constraints on past ice history.  
638 Therefore, our model results offer a different reconstruction to PATICE, and indicate that the ice

639 sheet in this region largely retreated by 15 ka, with only mountain glaciers remaining. This is  
640 supported further south, where the ice sheet disintegrated at ~16 ka with paleolake draining to the  
641 Pacific Ocean (~43° S, Leger et al., 2021a) and the ice remaining limited to higher mountain areas.  
642 However, during this interval, the Antarctic Cold Reversal (ACR) may have influenced the heat  
643 and hydrologic budget across this region, with wetter and cooler conditions interrupting the  
644 deglacial warming (Moreno et al., 2018). While TraCE-21ka simulates a cooler and wetter ACR,  
645 it is short-lived, lasting about 500 years as compared to 2,000 years in some ice core records or  
646 proxy-based studies (Lowry et al., 2019; He et al., 2013, Pedro et al., 2015). This potential for a  
647 favorable and prolonged period of glacier growth is likely missing in our simulations during the  
648 ACR.

### 649 **4.3 Limitations**

651  
652 Currently ISSM is undergoing model developments to include a full treatment of solid earth-ice  
653 and sea-level feedbacks (Adhikari et al., 2016). Therefore, at this time, there is no coupling  
654 between the ice sheet and solid earth. Instead, we prescribed GIA from a global GIA model of the  
655 last glacial cycle from Caron et al. (2018). While this model reasonably estimates GIA across the  
656 PIS over the last deglaciation, our simulated ice history does not feedback onto GIA. The ice  
657 history for Patagonia incorporated into the Caron et al. (2018) ensemble is from Ivins et al. 2011.  
658 Therefore, the prescribed GIA response across our domain does not perfectly match our simulated  
659 ice history. Additionally, the global mantle from Caron et al. (2018) does not exhibit regional low  
660 viscosity that is attributable to Patagonia and therefore, current rates of deformation are likely  
661 underestimated by the model. By not simulating the 2-way coupled ice and solid-earth  
662 interactions, we could be missing some feedbacks between our simulated ice history and the solid  
663 earth that may modulate the deglaciation across this region. Despite this limitation however, our  
664 prescribed GIA from Caron et al. (2018) is reasonable when compared with reconstructed deglacial  
665 GIA in Patagonia (Troch et al., 2022; see Figure S2), giving confidence that our simulation is  
666 capturing the regional influence of GIA on the simulated ice history.

667  
668 Across most of our domain, moraines formed of glacio-tectonized outwash (Bentley, 1996)  
669 provide evidence for an advance of piedmont glaciers across glacial outwash during the LGM,  
670 which formed the physical boundary for some of the existing terminal moraines around the lakes  
671 within the CLD (Bentley, 1996; Bentley, 1997). The formation of ice-contact proglacial lakes  
672 likely occurred as a function of deglacial warming as ice retreated into overdeepenings in the  
673 bedrock topography and filled with meltwater (Bentley, 1996). Where there were proglacial lakes  
674 along the westward ice front in the CLD, evidence suggests that ice was grounded during the LGM  
675 (Lago Puyehue; Heirman et al., 2011). During deglaciation, proglacial lakes formed along the ice  
676 sheet margin (Bentley 1996,1997; Davies et al., 2020), with evidence suggesting that local  
677 topography and calving may have influenced the spatially varying retreat rates along these margins  
678 (Bentley, 1997). Recent glacier modelling (Sutherland et al., 2020) suggests that inclusion of ice-  
679 lake interactions may have large impacts on the magnitude and rate of simulated ice front retreat,  
680 as ice-lake interactions promote greater ice velocities, ice flux to the grounding line, and surface  
681 lowering. However, it is not well constrained how the proglacial lakes in the CLD may have  
682 influenced local deglaciation (Heirman et al., 2011). While more geomorphic data is needed,  
683 recent work south of our study region (46.5°S) reconstructed early deglacial ice retreat using a  
684 glaciolacustrine varve record from Lago General Carrera-Buenos Aires (Bendle et al., 2019). The

685 authors find that following initial retreat due to deglacial warming, the ice margin retreated into a  
686 deepening proglacial lake which accelerated ice retreat in this region due to persistent calving,  
687 therefore supporting the role proglacial lakes likely played across the margins of the retreating PIS  
688 during the last deglaciation. Because the inclusion of ice-lake interactions is relatively novel for  
689 numerical ice flow modeling (Sutherland et al., 2020; Quiquet et al., 2021; Hinck et al., 2022), we  
690 choose to not simulate the evolution and influence of proglacial lakes on the deglaciation across  
691 this model domain. Given this limitation, our simulated magnitude and rate of ice retreat at the  
692 onset of deglaciation may be underestimated, especially when looking at local deglaciation along  
693 these proglacial lakes. Although we do not think that these processes would greatly influence our  
694 conclusions regarding the role of climate on the evolution of the PIS is the CLD and the simulated  
695 ice retreat history, future work is required to assess the influence of proglacial lakes in this region.  
696

## 697 **5 Conclusions**

698  
699 In this study, we use a numerical ice sheet model to simulate the LGM and deglacial ice history  
700 across the northernmost extent of the PIS, the CLD. The ice sheet model used inputs of  
701 temperature and precipitation from the TraCE-21ka climate model simulation covering the last  
702 22,000 years in order to simulate the deglaciation of the PIS across the CLD into the early  
703 Holocene.  
704

705 Our numerical simulation suggests that large scale ice retreat occurs after 19 ka coincident with  
706 rapid deglacial warming, with the northern portion of the CLD becoming ice free by 17 ka. The  
707 simulated ice retreat agrees well with the most comprehensive geologic assessment of past PIS  
708 history available (PATICE; Davies et al., 2020) for the LGM ice extent and early deglacial but  
709 diverge when considering the ice geometry at and after 15 ka. In our simulations, the PIS persists  
710 until 15 ka across the remainder of the CLD, followed by ice retreat to higher elevations as  
711 mountain glaciers and small ice caps persist into the early Holocene (e.g., Cerro Tronador). The  
712 geologic reconstruction from PATICE instead estimates a small ice cap persisting across the  
713 southern portion of high terrain in the CLD until about 10 ka. However, of the limited geologic  
714 constraints particularly after 15 ka, high uncertainty in the timing and extent of deglacial ice history  
715 remains in the geologic reconstruction. Therefore, our results provide an additional reconstruction  
716 of the deglaciation of the PIS across the CLD that differs from PATICE after 15 ka, emphasizing  
717 a need for future work that aims to improve geologic reconstructions of past ice margin migration  
718 particularly during the later deglaciation across this region.  
719

720 While deglacial warming was a primary driver of the demise of the PIS across the last deglaciation,  
721 we find that precipitation modulates the pacing and magnitude of deglacial ice retreat across the  
722 CLD. Paleoclimate proxies within the CLD has shown that the strength and position of the SWW  
723 varied during the LGM and last deglaciation, altering hydrologic patterns and influencing the  
724 deglacial mass balance. We find that the simulated changes in the strength and position of the  
725 SWW in TraCE-21ka are similar to those inferred from paleoclimate proxies of precipitation,  
726 consistent with a wetter than preindustrial climate being simulated and reconstructed over the CLD  
727 and in particular the region north of 40°S. Through a series of sensitivity tests, we alter the  
728 magnitude of the precipitation anomaly modestly (up to 10%) during our transient deglacial  
729 simulations and find that the pacing of ice retreat can speed up or slow down by a few hundred  
730 years and up to 2000 years depending on the imposed increase or decrease in the precipitation

731 anomaly. While paleoclimate proxies of precipitation suggest that the CLD may have experienced  
732 twice as much precipitation during the LGM and early deglacial relative to present day (Moreno  
733 et al.,1999;2015), TraCE-21ka simulates smaller increases in LGM and early deglacial  
734 precipitation (~10-15% greater than preindustrial). Therefore, while our modelling suggests that  
735 modest changes in precipitation can modulate the pace of deglacial ice retreat across the CLD,  
736 from our analysis we can deduce that larger anomalies in precipitation as found in the paleoclimate  
737 proxies may have an even larger impact on modulating deglacial ice retreat. Because paleoclimate  
738 proxies of past precipitation are often lacking, and climate models can simulate a range of possible  
739 LGM and deglacial hydrologic states, these results suggest that improved knowledge of the past  
740 precipitation is critical towards better understanding the drivers of PIS growth and demise,  
741 especially as small variations in precipitation can modulate ice sheet history on scales consistent  
742 with geologic proxies.

743

#### 744 **Code/Data Availability**

745 The simulations performed for this paper made use of the open-source Ice-Sheet and Sea-level  
746 System Model (ISSM) and are publicly available at <https://issm.jpl.nasa.gov/> (Larour et al., 2012).

747

#### 748 **Author Contribution**

749 JC and SM secured funding for this research. JC, MR, and SM all contributed to the project design.  
750 JC performed the model setup and simulations. JC performed the analyses on model output, with  
751 help from MR who performed analysis on PATICE reconstructions. JC wrote the manuscript with  
752 input from MR and SM.

753

#### 754 **Competing interests**

755 The contact author has declared that none of the authors has any competing interests.

756

#### 757 **Acknowledgements**

758 This work was supported by a grant from the National Science Foundation, Frontier Research in  
759 Earth Sciences # 2121561. We would like to thank Lambert Caron from the Jet Propulsion  
760 Laboratory for his input regarding Glacial Isostatic Adjustment across our study region.

761

#### 762 **References**

763 Adhikari, S., Ivins, E. R., and Larour, E., 2016, ISSM-SESAW v1.0: mesh-based computation of  
764 gravitationally consistent sea level and geodetic signatures caused by cryosphere and  
765 climate driven mass change, *Geoscientific Model Development*, 9, 9769-9816, doi:  
766 10.5194/gmd-9-1087-2016.

767 Åkesson, H., Morlighem, M., Nisancioglu, K. H., Svendsen, J. J., and Mangerud, J.:  
768 Atmosphere-driven ice sheet mass loss paced by topography: Insights from modelling the  
769 south-western Scandinavian Ice Sheet. 2018. *Quaternary Sci. Rev.*, 195, 32–  
770 47, <https://doi.org/10.1016/j.quascirev.2018.07.004>.

771 Andersen, B., Denton, G. H., & Lowell, T. V. (1999). Glacial geomorphologic maps of  
772 Llanquihue drift in the area of the southern Lake District, Chile. *Geografiska Annaler:*  
773 *Series A, Physical Geography*, 81(2), 155-166.

774 Bendle, J.M., Palmer, A.P., Thorndycraft, V.R., Matthews, I.P. 2019. Phased Patagonian Ice  
775 Sheet response to Southern Hemisphere atmospheric and oceanic warming between 18  
776 and 17 ka. *Sci. Rep.* 9, 4133. <https://doi.org/10.1038/s41598-019-39750-w>

777 Bentley, M.J., 1996. The role of lakes in moraine formation, Chilean Lake District. *Earth*  
778 *Surf. Process. Landf.* 21, 493–507. [https://doi.org/10.1002/\(SICI\)1096-](https://doi.org/10.1002/(SICI)1096-)  
779 9837(199606)21:6<493::AID-ESP612>3.0.CO;2-D

780 Bentley, M.J., 1997. Relative and radiocarbon chronology of two former glaciers in the  
781 Chilean Lake District. *J. Quat. Sci.* 12, 25–33. [https://doi.org/10.1002/\(SICI\)1099-](https://doi.org/10.1002/(SICI)1099-)  
782 1417(199701/02)12:1<25::AID-JQS289>3.0.CO;2-A

783 Berman, L., Silvestri, G., Tonello, M.S., On differences between Last Glacial Maximum and  
784 Mid-Holocene climates in southern South America simulated by PMIP3 models. 2018.  
785 *Quat. Sci. Rev.* 185. 113-121. <https://doi.org/10.1016/j.quascirev.2018.02.003>.

786 Blatter, H.: Velocity and stress-fields in grounded glaciers: A simple algorithm for including  
787 deviatoric stress gradients. 1995. *J. Glaciol.*, 41, 333-344,  
788 <https://doi.org/10.3189/S002214300001621X>

789 Boex, J., Fogwill, C., Harrison, S. et al. Rapid thinning of the late Pleistocene Patagonian Ice  
790 Sheet followed migration of the Southern Westerlies. 2013. *Sci Rep* 3, 2118.  
791 <https://doi.org/10.1038/srep02118>

792 Boisier, J. P., Alvarez-Garretón, C., Cepeda, J., Osses, A., Vásquez, N., and Rondanelli, R.:  
793 CR2MET: A high-resolution precipitation and temperature dataset for hydroclimatic  
794 research in Chile. 2018. EGUGA, p. 19739.

795 Braun, M.H., Malz, P., Sommer, C., Far.as-Barahona, D., Sauter, T., Casassa, G., Soruco,  
796 A., Skvarca, P., Seehaus, T.C., 2019. Constraining glacier elevation and mass changes  
797 in South America. *Nat. Clim. Chang.* 9, 130–136. <https://doi.org/10.1038/s41558-018->  
798 0375-7

799 Brierley, C. M., Zhao, A., Harrison, S. P., Braconnot, P., Williams, C. J. R., Thornalley, D. J. R.,  
800 Shi, X., Peterschmitt, J.-Y., Ohgaito, R., Kaufman, D. S., Kageyama, M., Hargreaves, J.  
801 C., Erb, M. P., Emile-Geay, J., D'Agostino, R., Chandan, D., Carré, M., Bartlein, P. J.,  
802 Zheng, W., Zhang, Z., Zhang, Q., Yang, H., Volodin, E. M., Tomas, R. A., Routson, C.,  
803 Peltier, W. R., Otto-Bliesner, B., Morozova, P. A., McKay, N. P., Lohmann, G., Legrande,  
804 A. N., Guo, C., Cao, J., Brady, E., Annan, J. D., and Abe-Ouchi, A.: Large-scale features  
805 and evaluation of the PMIP4-CMIP6 *midHolocene* simulations, *Clim. Past*, 16, 1847–  
806 1872, <https://doi.org/10.5194/cp-16-1847-2020>, 2020.

807 Briner, J. P., Cuzzone, J. K., Badgley, J. A., Young, N. E., Steig, E. J., Morlighem, M.,  
808 Schlegel, N.-J., Hakim, G., Schaefer, J. Johnson, J. V., Lesnek, A. L., Thomas, E. K.,  
809 Allan, E., Bennike, O., Cluett, A. A., Csatho, B., de Vernal, A., Downs, J., Larour, E.,  
810 and Nowicki, S.: Rate of mass loss from the Greenland Ice Sheet will exceed Holocene  
811 values this century. 2020. *Nature*, 6, 70–74, <https://doi.org/10.1038/s41586-020-2742-6>.

812 Bondzio, J. H., Seroussi, H., Morlighem, M., Kleiner, T., Rückamp, M., Humbert, A., and  
813 Larour, E. Y.: Modelling calving front dynamics using a level-set method: application to  
814 Jakobshavn Isbræ, West Greenland. 2016. *The Cryosphere*, 10, 497–  
815 510, <https://doi.org/10.5194/tc-10-497-2016>

816 Budd, W.F., P. L. Keage, N. A. Blundy. Empirical studies of ice sliding. 1979. *J. Glaciol.*,  
817 23:157-170.

818 Caron, L., Ivins, E. R., Larour, E., Adhikari, S., Nilsson, J., and Blewitt, G.: GIA model statistics  
819 for GRACE hydrology, cryosphere and ocean science. 2018. *Geophys. Res. Lett.*, 45,  
820 2203–2212, <https://doi.org/10.1002/2017GL076644>

821 Choi, Y., Morlighem, M., Rignot, E., and Wood, M.: Ice dynamics will remain a primary driver

822 of Greenland ice sheet mass loss over the next century. 2021. *Commun. Earth Environ.*,  
823 2, 26, <https://doi.org/10.1038/s43247-021-00092-z>

824 Clark, P.U., He, F., Gollledge, N.R., Mitrovica, J.X., Dutton, A., Hoffman, J.S., and Dendy, S.,  
825 2020, Oceanic forcing of penultimate deglacial and last interglacial sea-level rise: *Nature*,  
826 v. 577, p. 660–664, doi:10.1038/s41586-020-1931-7.

827 Cuffey, K. M. and Paterson, W. S. B.: *The physics of glaciers*, 4th edn. 2010. Butterworth-  
828 Heinemann, Oxford, ISBN 9780123694614

829 Cuzzone, J. K., Schlegel, N.-J., Morlighem, M., Larour, E., Briner, J. P., Seroussi, H., and Caron,  
830 L.: The impact of model resolution on the simulated Holocene retreat of the southwestern  
831 Greenland ice sheet using the Ice Sheet System Model (ISSM). 2019. *The Cryosphere*,  
832 13, 879–893, <https://doi.org/10.5194/tc-13-879-2019>.

833 Cuzzone, J. K., Young, N. E., Morlighem, M., Briner, J. P., and Schlegel, N.-J.: Simulating the  
834 Holocene deglaciation across a marine-terminating portion of southwestern Greenland in  
835 response to marine and atmospheric forcings. 2022. *The Cryosphere*, 16, 2355–2372,  
836 <https://doi.org/10.5194/tc-16-2355-2022>.

837 Davies, B.J., Darvill, C.M., Lovell, H., Bendle, J.M., Dowdeswell, J.A., Fabel, D.,  
838 Gheorghiu, D.M., 2020. The evolution of the Patagonian ice sheet from 35 ka to  
839 the present day (PATICE). *Earth Sci. Rev.* 204, 103152. [https://doi.org/10.1016/](https://doi.org/10.1016/j.earscirev.2020.103152)  
840 [j.earscirev.2020.103152](https://doi.org/10.1016/j.earscirev.2020.103152).

841 Darvill, C.M., Stokes, C.R., Bentley, M.J., Evans, D.J.A., Lovell, H. 1996. Dynamics of former  
842 ice lobes of the southernmost Patagonian Ice Sheet based on glacial landsystems  
843 approach. *Journal of Quaternary Science.* 32, 6, 857-876.  
844 <https://doi.org/10.1002/jqs.2890>

845 Darvill, C.M., Stokes, C.R., Bentley, M.J., Evans, D.J.A., Lovell, H., Dynamics of former ice  
846 lobes of the southernmost Patagonian Ice Sheet based on glacial landsystems approach.  
847 2017. *J. Quaternary Sci.*, 32:857-876. <https://doi.org/10.1002/jqs.2890>

848 Denton, G.H., Lowell, T.V., Heusser, C.J., Schlüchter, C., Andersen, B.G., Heusser, L.E.,  
849 Moreno, P.I., Marchant, D.R., 1999. Geomorphology, Stratigraphy, and Radiocarbon  
850 Chronology of Llanquihue Drift in the Area of the Southern Lake District, Seno  
851 Reloncav., and Isla Grande de Chilo., Chile. *Geogr. Ann. Ser. A Phys. Geogr.* 81,  
852 167–229. <https://doi.org/10.1111/1468-0459.00057>

853 Denton, G.H., Heusser, J., Lowell, T.V., Moreno, P.I., Andersen, B.G., Heusser, L.E., Schlüchter,  
854 C., Marchant, D.R. 1999. Interhemispheric Linkage of Paleoclimate During the Last  
855 Glaciation. *Geografiska Annaler.* 81, 2, 107-153. [https://doi.org/10.1111/1468-](https://doi.org/10.1111/1468-0459.00055)  
856 [0459.00055](https://doi.org/10.1111/1468-0459.00055)

857 Dias dos Santos, T., Morlighem, M., and Brinkerhoff, D.: A new vertically integrated MONo-  
858 Layer Higher-Order (MOLHO) ice flow model. 2022. *The Cryosphere*, 16, 179–195,  
859 <https://doi.org/10.5194/tc-16-179-2022>.

860 Díaz, C., Moreno, P. I., Villacís, L. A., Sepúlveda-Zúñiga, E. A., & Maidana, N. I. (2023).  
861 Freshwater diatom evidence for Southern Westerly Wind evolution since ~ 18 ka in  
862 northwestern Patagonia. *Quaternary Science Reviews*, 316, 108231.

863 Fernandez, A., Mark, B.G. 2016. Modeling modern glacier response to climate changes along the  
864 Andes Cordillera: A multiscale review, *J. Adv. Model. Earth Syst.*, 8, 467–495,  
865 doi:10.1002/2015MS000482.

866 García, J. L., Maldonado, A., De Porrás, M. E., Delaunay, A. N., Reyes, O., Ebensperger, C. A.,  
867 Binnie, Lüthgens, C., S.A., Méndez, C. 2019. Early deglaciation and paleolake history of



868 Río Cisnes glacier, Patagonian ice sheet (44 S). *Quaternary Research*, 91(1), 194-217.  
869 <https://doi.org/10.1017/qua.2018.93>.  
870

871 Garreaud, R., Lopez, P., Minvielle, M., & Rojas, M. (2013). Large-scale control on the  
872 Patagonian climate. *Journal of Climate*, 26(1), 215-230.

873 GEBCO Bathymetric Compilation Group 2021. 2021. The GEBCO\_2021 Grid - a continuous  
874 terrain model of the global oceans and land. NERC EDS British Oceanographic Data  
875 Centre NOC. doi:10.5285/c6612cbe-50b3-0cff-e053-6c86abc09f8f

876 Glasser, N. F., Jansson, K. N., Harrison, S., & Kleman, J. (2008). The glacial geomorphology  
877 and Pleistocene history of South America between 38 S and 56 S. *Quaternary Science*  
878 *Reviews*, 27(3-4), 365-390.

879 Glen, J. W. The creep of polycrystalline ice. 1955. *P. Roy. Soc. Lond. A*, 228, 519–  
880 538, <https://doi.org/10.1098/rspa.1955.0066>.

881 Golledge, N. R., Thomas, Z. A., Levy, R. H., Gasson, E. G. W., Naish, T. R., McKay, R. M.,  
882 Kowalewski, D. E., and Fogwill, C. J.: Antarctic climate and ice-sheet configuration  
883 during the early Pliocene interglacial at 4.23 Ma, *Clim. Past*, 13, 959–975,  
884 <https://doi.org/10.5194/cp-13-959-2017>, 2017.

885 Hartmann, D. and Lo, F. Wave-Driven Zonal Flow Vacillation in the Southern Hemisphere.  
886 1998. *Journal of the Atmospheric Sciences*. 55, 8, 1303-1315.  
887 [https://doi.org/10.1175/1520-0469\(1998\)055<1303:WDZFVI>2.0.CO;2](https://doi.org/10.1175/1520-0469(1998)055<1303:WDZFVI>2.0.CO;2)

888 Hajima, T., Watanabe, M., Yamamoto, A., Tatebe, H., Noguchi, M. A., Abe, M., Ohgaito, R.,  
889 Ito, A., Yamazaki, D., Okajima, H., Ito, A., Takata, K., Ogochi, K., Watanabe, S., and  
890 Kawamiya, M.: Development of the MIROC-ES2L Earth system model and the  
891 evaluation of biogeochemical processes and feedbacks, *Geosci. Model Dev.*, 13, 2197–  
892 2244, <https://doi.org/10.5194/gmd-13-2197-2020>

893 He, F., Shakun, J. D., Clark, P. U., Carlson, A. E., Liu, Z., Otto-Bliesner, B. L., Kutzbach, J. E.  
894 2013. Northern Hemisphere forcing of Southern Hemisphere climate during the last  
895 deglaciation, *Nature*, 494, 81–85. doi: 10.1038/nature11822.

896 He, F., Clark, P.U. 2022. Freshwater forcing of the Atlantic Meridional Overturning Circulation  
897 revisited. *Nature Climate Change*. 12. 449-454. [https://doi.org/10.1038/s41558-022-](https://doi.org/10.1038/s41558-022-01328-2)  
898 [01328-2](https://doi.org/10.1038/s41558-022-01328-2).

899 Heirman, K., De Batist, M., Charlet, F., Moernaut, J., Chapron, E., Brümmer, R., Pino, M.,  
900 Urrutia, R., 2011. Detailed seismic stratigraphy of Lago Puyehue: implications for the  
901 mode and timing of glacier retreat in the Chilean Lake District. *J. Quat. Sci.* 26,  
902 665–674. <https://doi.org/10.1002/jqs.1491>

903 Hinck, S., Gowan, E. J., Zhang, X., and Lohmann, G.: PISM-LakeCC: Implementing an adaptive  
904 proglacial lake boundary in an ice sheet model. 2022. *The Cryosphere*, 16, 941–965,  
905 <https://doi.org/10.5194/tc-16-941-2022>.

906 Hubbard, A., Hein, A.S., Kaplan, M.R., Hulton, N.R.J., Glasser, N., 2005. A modelling  
907 reconstruction of the last glacial maximum ice sheet and its deglaciation in the  
908 vicinity of the northern patagonian icefield, south America. *Geogr. Ann. Phys.Geogr.* 87  
909 (2), 375-391. <https://doi.org/10.1111/j.0435-3676.2005.00264.x>

910 Hulton, N.R.J., Purves, R., McCulloch, R., Sugden, D.E., Bentley, M.J., 2002. The last  
911 glacial maximum and deglaciation in southern south America. *Quat. Sci. Rev.* 21  
912 (1), 233-241. [https://doi.org/10.1016/S0277-3791\(01\)00103-2](https://doi.org/10.1016/S0277-3791(01)00103-2).

913 Hulton, N., Sugden, D., Payne, A., Clapperton, C., 1994. Glacier modeling and the

914 climate of Patagonia during the last glacial maximum. *Quat. Res.* 42 (1), 1-19.  
915 doi:10.1006/qres.1994.1049

916 Jiang, N., Yan, Q. Evolution of the meridional shift of the subtropical and subpolar westerly jet  
917 over the Southern Hemisphere during the past 21,000 years. 2020. *Quat Sci. Rev.* 246,  
918 <https://doi.org/10.1016/j.quascirev.2020.106544>.

919 Kaplan, M. R., Ackert Jr, R. P., Singer, B. S., Douglass, D. C., & Kurz, M. D. 2004. Cosmogenic  
920 nuclide chronology of millennial-scale glacial advances during O-isotope stage 2 in  
921 Patagonia. *Geological Society of America Bulletin*, 116(3-4), 308-321. doi:  
922 10.1130/B25178.1

923 Kaplan, M. R., Fogwill, C. J., Sugden, D. E., Hulton, N. R. J., Kubik, P. W., & Freeman, S. P. H.  
924 T. 2008. Southern Patagonian glacial chronology for the Last Glacial period and  
925 implications for Southern Ocean climate. *Quaternary Science Reviews*, 27(3-4), 284-294.  
926 <https://doi.org/10.1016/j.quascirev.2007.09.013>

927 Kilian, R., Lamy, F., 2012. A review of Glacial and Holocene paleoclimate records  
928 from southernmost Patagonia (49e55 S). *Quat. Sci. Rev.* 53,  
929 doi.10.1016/j.quascirev.2012.07.017

930 Kageyama, M., Harrison, S. P., Kapsch, M.-L., Lofverstrom, M., Lora, J. M., Mikolajewicz, U.,  
931 Sherriff-Tadano, S., Vadsaria, T., Abe-Ouchi, A., Bouttes, N., Chandan, D., Gregoire, L.  
932 J., Ivanovic, R. F., Izumi, K., LeGrande, A. N., Lhardy, F., Lohmann, G., Morozova, P.  
933 A., Ohgaito, R., Paul, A., Peltier, W. R., Poulsen, C. J., Quiquet, A., Roche, D. M., Shi,  
934 X., Tierney, J. E., Valdes, P. J., Volodin, E., and Zhu, J. 2021. The PMIP4 Last Glacial  
935 Maximum experiments: preliminary results and comparison with the PMIP3 simulations,  
936 *Clim. Past*, 17, 1065–1089, <https://doi.org/10.5194/cp-17-1065-2021>.

937 Kilian, R., Lamy, F. A review of Glacial and Holocene paleoclimate records from southernmost  
938 Patagonia (49-55°S). 2012. 53, 15, 1-23.  
939 <https://doi.org/10.1016/j.quascirev.2012.07.017>

940 Kohfeld, K.E., Graham, R.M., Boer, A. M. de, Sime, L.C., Wolff, E.W., Qu er e, C.L.,  
941 Bopp, L., 2013. Southern Hemisphere westerly wind changes during the Last  
942 Glacial Maximum: paleo-data synthesis. *Quat. Sci. Rev.* 68, 76-95. ,  
943 10.1016/j.quascirev.2013.01.017

944 Lamy, F., Kilian, R., Arz, H.W., Francois, J.-P., Kaiser, J., Prange, M., Steinke, T., 2010.  
945 Holocene changes in the position and intensity of the southern westerly wind belt. *Nat.*  
946 *Geosci.* 3, 695–699. <https://doi.org/10.1038/ngeo959>

947 Lamy, F., Arz, H. W., Kilian, R., Lange, C. B., Lembke-Jene, L., Wengler, M., ... & Tiedemann,  
948 R. (2015). Glacial reduction and millennial-scale variations in Drake Passage  
949 throughflow. *Proceedings of the National Academy of Sciences*, 112(44), 13496-13501  
950 <https://doi.org/10.1073/pnas.1509203112>

951 Larour, E., Seroussi, H., Morlighem, M., and Rignot, E.: Continental scale, high order, high  
952 spatial resolution, ice sheet modeling using the Ice Sheet System Model (ISSM). 2012. *J.*  
953 *Geophys. Res.-Earth*, 117, F01022, <https://doi.org/10.1029/2011JF002140>

954 Le Morzadec, K., Tarasov, L., Morlighem, M., and Seroussi, H.: A new sub-grid surface mass  
955 balance and flux model for continental-scale ice sheet modelling: testing and last glacial  
956 cycle. 2015. *Geosci. Model Dev.*, 8, 3199–3213, [https://doi.org/10.5194/gmd-8-3199-](https://doi.org/10.5194/gmd-8-3199-2015)  
957 2015

958 Leger, T. P., Hein, A. S., Bingham, R. G., Rodés, Á., Fabel, D., & Smedley, R. K. 2021a.  
959 Geomorphology and <sup>10</sup>Be chronology of the Last Glacial Maximum and deglaciation in

- 960 northeastern Patagonia, 43° S-71° W. *Quaternary Science Reviews*, 272, 107194.  
 961 DOI:[10.1016/j.quascirev.2021.107194](https://doi.org/10.1016/j.quascirev.2021.107194)
- 962 Leger TPM, Hein AS, Goldberg D, Schimmelpfennig I, Van Wyk de Vries MS, Bingham RG and  
 963 ASTER Team. 2021b. Northeastern Patagonian Glacier Advances (43°S) Reflect  
 964 Northward Migration of the Southern Westerlies Towards the End of the Last Glaciation.  
 965 *Front. Earth Sci.* 9:751987. doi: 10.3389/feart.2021.751987
- 966 Liu, Z., Otto-Bliesner, B., He, F., Brady, E., Tomas, R., Clark, P., Carlson, A., Lynch-Stieglitz,  
 967 J., Curry, W., Brook, E., Erickson, D., Jacob, R., Kutzbach, J., and Cheng, J. 2009.  
 968 Transient simulation of last deglaciation with a new mechanism for Bølling-Allerød  
 969 warming, *Science*, 325, 310–314. <https://doi.org/10.1126/science.1171041>
- 970 Lowry, D. P., Golledge, N. R., Menviel, L., and Bertler, N. A. N.: Deglacial evolution of  
 971 regional Antarctic climate and Southern Ocean conditions in transient climate  
 972 simulations. 2019. *Clim. Past*, 15, 189–215, <https://doi.org/10.5194/cp-15-189-2019>.
- 973 Lowell, T., Heusser, C., Andersen, B., Moreno, P., Hauser, A., Heusser, L., Schlüchter,  
 974 C., Marchant, D., Denton, G., 1995. Interhemispheric correlation of late Pleistocene glacial  
 975 events. *Science* 269, 1541–1549. Doi: 10.1126/science.269.5230.1541
- 976 Lowry, D. P., Golledge, N. R., Menviel, L., and Bertler, N. A. N.: Deglacial evolution of  
 977 regional Antarctic climate and Southern Ocean conditions in transient climate  
 978 simulations. 2019. *Clim. Past*, 15, 189–215, <https://doi.org/10.5194/cp-15-189-2019>
- 979 Marcott, S.A., Shakun, J.D., Clark, P.U., Mix, A.C. 2013. A Reconstruction of Regional and  
 980 Global Temperature for the Past 11,300 Years. 339, 6124, 1198-1201. DOI:  
 981 10.1126/science.1228026
- 982 Martin J, Davies BJ, Jones R and Thorndycraft V (2022), Modelled sensitivity of Monte San  
 983 Lorenzo ice cap, Patagonian Andes, to past and present climate. *Front. Earth Sci.*  
 984 10:831631. doi: 10.3389/feart.2022.831631
- 985 Mauritsen, T., Bader, J., Becker, T., Behrens, J., Bittner, M., Brokopf, R., Brovkin, V., Claussen,  
 986 M., Crueger, T., Esch, M., Fast, I., Fiedler, S., Fläschner, D., Gayler, V., Giorgetta, M.,  
 987 Goll, D. S., Haak, H., Hagemann, S., Hedemann, C., Hohenegger, C., Ilyina, T., Jahns, T.,  
 988 Jimenez-de-la-Cuesta, D., Jungclaus, J., Kleinen, T., Kloster, S., Kracher, D., Kinne, S.,  
 989 Kleberg, D., Lasslop, G., Kornbluh, L., Marotzke, J., Matei, D., Meraner, K.,  
 990 Mikolajewicz, U., Modali, K., Möbis, B., Müller, W. A., Nabel, J. E. M. S., Nam, C. C.  
 991 W., Notz, D., Nyawira, S.-S., Paulsen, H. Peters, K., Pincus, R., Pohlmann, H. Pongratz,  
 992 J., Popp, M., Raddatz, T. J., Rast, S., Redler, R., Reick, C. H., Rohrschneider, T.,  
 993 Schemann, V., Schmidt, H., Schnur, R., Schulzweida, U., Six, K. D., Stein, L., Stemmler,  
 994 I., Stevens, B., von Storch, J.-S., Tian, F., Voigt, A., Vrese, P., Wieners, K.-H.,  
 995 Wilkenskjaeld, S., Winkler, A., and Roeckner, E.: Developments in the MPI-M Earth  
 996 System Model version 1.2 (MPI-ESM1.2) and its response to increasing CO<sub>2</sub>, *J. Adv.*  
 997 *Model. Earth Syst.* 2019. 11, 998–1038, <https://doi.org/10.1029/2018MS001400>
- 998 McCulloch, R. D., Bentley, M. J., Purves, R. S., Hulton, N. R., Sugden, D. E., & Clapperton, C.  
 999 M. (2000). Climatic inferences from glacial and palaeoecological evidence at the last  
 1000 glacial termination, southern South America. *Journal of Quaternary Science: Published*  
 1001 *for the Quaternary Research Association*, 15(4), 409-417.  
 1002 <https://doi.org/10.1002/jqs.608>
- 1003 McCulloch, R. D., Fogwill, C. J., Sugden, D. E., Bentley, M. J., & Kubik, P. W. (2005).  
 1004 Chronology of the last glaciation in central Strait of Magellan and Bahía Inútil,

1005 southernmost South America. *Geografiska Annaler: Series A, Physical*  
1006 *Geography*, 87(2), 289-312. <https://doi.org/10.1111/j.0435-3676.2005.00260.x>

1007 Meier, W.J-H., Griesinger, J., Hochreuther, P., Braun, M.H. 2018. An updated multi-temporal  
1008 glacier inventory for the Patagonian Andes with changes between the Little Ice Age and  
1009 2016. *Frontiers in Earth Science*, 6, 62. <https://doi.org/10.3389/feart.2018.00062>

1010 Meniel, L., A. Timmermann, A. Mouchet, and O. Timm, 2008: Climate and marine carbon  
1011 cycle response to changes in the strength of the Southern Hemispheric  
1012 westerlies. *Paleoceanography*, 23, PA4201, doi:10.1029/2008PA001604.

1013 Mercer, J.H., 1972. Chilean glacial chronology 20,000 to 11,000 carbon-14 years ago:some  
1014 global comparisons. *Science* 176, 1118–1120. DOI: 10.1126/science.176.4039.1118

1015 Moreno, P. I., Lowell, T. V., Jacobson Jr, G. L., & Denton, G. H. (1999). Abrupt vegetation and  
1016 climate changes during the last glacial maximum and last termination in the Chilean lake  
1017 district: a case study from Canal de la Puntilla (41°S). *Geografiska Annaler: Series A,*  
1018 *Physical Geography*, 81(2), 285-311.

1019 Moreno, P.I., Denton, G.H., Moreno, H., Lowell, T.V., Putnam, A.E., Kaplan, M.R., 2015.  
1020 Radiocarbon chronology of the last glacial maximum and its termination in  
1021 northwestern Patagonia. *Quat. Sci. Rev.* 122, 233e249. 10.1016/j.quascirev.2015.05.027

1022 Moreno, P.I., Videla, J., Valero-Garcés, B.L., Alloway, B.V., Heusser, L.E., 2018.  
1023 A continuous record of vegetation, fire-regime and climatic changes in northwestern  
1024 Patagonia spanning the last 25,000 years. *Quat. Sci. Rev.* 198,  
1025 10.1016/j.quascirev.2018.08.013

1026 Morlighem, M., Bondzio, J., Seroussi, H., Rignot, E., Larour, E., Humbert, A., and Rebuffi, S.:  
1027 Modeling of Store Gletscher's calving dynamics, West Greenland, in response to ocean  
1028 thermal forcing. 2016. *Geophys. Res. Lett.*, 43, 2659–  
1029 2666, <https://doi.org/10.1002/2016GL067695>

1030 Muir, R., Eaves, S., Vargo, L., Anderson, B., Mackintosh, A., Sagredo, E., Soteres, R. Late  
1031 glacial climate evolution in the Patagonian Andes (44-47°S) from alpine glacier modelling.  
1032 2023. *Quaternary Science Reviews*, 305, <https://doi.org/10.1016/j.quascirev.2023.108035>.

1033 Ohgaito, R., Yamamoto, A., Hajima, T., Oishi, R., Abe, M., Tatebe, H., Abe-Ouchi, A., and  
1034 Kawamiya, M.: PMIP4 experiments using MIROC-ES2L Earth system model, *Geosci.*  
1035 *Model Dev.*, 14, 1195–1217, <https://doi.org/10.5194/gmd-14-1195-2021>

1036 Pattyn, F.: A new three-dimensional higher-order thermomechanical ice sheet model:  
1037 Basic sensitivity, ice stream development, and ice flow across subglacial lakes. 2003. *J.*  
1038 *Geophys. Res.*, 108, 2382, <https://doi.org/10.1029/2002JB002329>

1039 Pedro, J. B., Bostock, H. C., Bitz, C. M., He, F., Vandergoes, M. J., Steig, E. J., Chase, B.M.,  
1040 Krause, C.E., Rasmussen, S.O., Bradley, M.R., Cortese, G. 2016. The spatial extent and  
1041 dynamics of the Antarctic Cold Reversal. *Nature Geoscience*, 9(1), 51-55.  
1042 <https://doi.org/10.1038/ngeo2580>

1043 Peixoto, J. P., and A. H. Oort (1992), *Physics of Climate*, American Institute of Physics,  
1044 520 pp.

1045 Peltier, C., Kaplan, M. R., Birkel, S. D., Soteres, R. L., Sagredo, E. A., Aravena, J. C., ... &  
1046 Schaefer, J. M. (2021). The large MIS 4 and long MIS 2 glacier maxima on the southern  
1047 tip of South America. *Quaternary Science Reviews*, 262, 106858.  
1048 <https://doi.org/10.1016/j.quascirev.2021.106858> 0277-3791

1049 Peltier, C., Kaplan, M. R., Sagredo, E. A., Araos, J., Birkel, S. D., ... & Schaefer,  
1050 J. M. (2023). The last two glacial cycles in central Patagonia: A precise record from the

1051 Ñirehuao glacier lobe. *Quaternary Science Reviews*, 304, 107873.  
1052 DOI:10.1016/j.quascirev.2022.107873  
1053  
1054 Pfeffer, W.T., Arendt, A.A., Bliss, A., Bolch, T., Cogley, J.G., Gardner, A.S., Hagen, J.O., Hock,  
1055 R., Kaser, G., Kienholz, C. and Miles, E.S. 2014. The Randolph Glacier Inventory: a  
1056 globally complete inventory of glaciers. *Journal of Glaciology*, 60, 537-552.  
1057 Doi:10.313189/2014JoG13J176  
1058 Pollard, D. and DeConto, R. M.: Description of a hybrid ice sheet-shelf model, and application to  
1059 Antarctica. 2012. *Geosci. Model Dev.*, 5, 1273–1295, [https://doi.org/10.5194/gmd-5-](https://doi.org/10.5194/gmd-5-1273-2012)  
1060 1273-2012.  
1061 Porter, S. C. (1981). Pleistocene glaciation in the southern Lake District of Chile. *Quaternary*  
1062 *Research*, 16(3), 263-292.  
1063 Quiquet, A., Dumas, C., Paillard, D., Ramstein, G., Ritz, C., and Roche, D. M.: Deglacial Ice  
1064 Sheet Instabilities Induced by Proglacial Lakes. 2021. *Geophys. Res. Lett.*, 48,  
1065 e2020GL092141, <https://doi.org/10.1029/2020GL092141>  
1066 Rojas, M., Moreno, P., Kageyama, M., Crucifix, M, Hewitt, C., Abe-Ouchi, A., Ohgaito, R.,  
1067 Brady, E.C., Hop, P. 2009. The Southern Westerlies during the last glacial maximum in  
1068 PMIP2 simulations. *Clim. Dyn.* 32, 525–548. [https://doi.org/10.1007/s00382-008-0421-](https://doi.org/10.1007/s00382-008-0421-7)  
1069 7.  
1070 Rojas, M., 2013. Sensitivity of southern Hemisphere circulation to LGM and 4 CO<sub>2</sub>  
1071 climates. *Geophys. Res. Lett.* 40, 965e970.  
1072 Sepulchre, P., Caubel, A., Ladant, J.-B., Bopp, L., Boucher, O., Braconnot, P., Brockmann, P.,  
1073 Cozic, A., Donnadieu, Y., Dufresne, J.-L., Estella-Perez, V., Ethé, C., Fluteau, F.,  
1074 Foujols, M.-A., Gastineau, G., Ghattas, J., Hauglustaine, D., Hourdin, F., Kageyama, M.,  
1075 Khodri, M., Marti, O., Meurdesoif, Y., Mignot, J., Sarr, A.-C., Servonnat, J.,  
1076 Swingedouw, D., Szopa, S., and Tardif, D.: IPSL-CM5A2 – an Earth system model  
1077 designed for multi-millennial climate simulations, *Geosci. Model Dev.*, 2020. 13, 3011–  
1078 3053, <https://doi.org/10.5194/gmd-13-3011-2020>  
1079 Seguinot, J., Rogozhina, I., Stroeven, A. P., Margold, M., and Kleman, J.: Numerical simulations  
1080 of the Cordilleran ice sheet through the last glacial cycle, *The Cryosphere*, 10, 639–664,  
1081 <https://doi.org/10.5194/tc-10-639-2016>, 2016.  
1082 Shakun, J., Clark, P., He, Marcott, S.A., Mix, A. C., Liu, A., Otto-Bliesner, B., Schmittner, A.,  
1083 Bards, E. 2012. Global warming preceded by increasing carbon dioxide concentrations  
1084 during the last deglaciation. *Nature* 484, 49–54. <https://doi.org/10.1038/nature10915>  
1085 Shakun, J.D., Lea, D.W., Lisiecki, L.E., Raymo, M.E. 2015. An 800-kyr record of global  
1086 surface ocean δ<sup>18</sup>O and implications for ice volume-temperature coupling. 426, 58-68.  
1087 <https://doi.org/10.1016/j.epsl.2015.05.042>  
1088 Sidorenko, D., Goessling, H., Koldunov, N., Scholz, P., Danilov, S., Barbi, D., Cabos, W.,  
1089 Gurses, O., Harig, S., Hinrichs, C., Juricke, S., Lohmann, G., Losch, M., Mu, L.,  
1090 Rackow, T., Rakowsky, N., Sein, D., Semmler, T., Shi, X., Stepanek, C., Streffing, J.,  
1091 Wang, Q., Wekerle, C., Yang, H., and Jung, T.: Evaluation of FESOM2.0 Coupled to  
1092 ECHAM6.3: Preindustrial and High- ResMIP Simulations, 2019. *J. Adv. Model. Earth*  
1093 *Sy.*, 11, 3794–3815, <https://doi.org/10.1029/2019MS001696>  
1094 Sime, L. C., K. E. Kohfeld, C. Le Quéré, E. W. Wolff, A. M. de Boer, R. M. Graham,  
1095 and L. Bopp, 2013: Southern Hemisphere westerly wind changes during the Last Glacial

1096 Maximum: Model–data comparison. *Quat. Sci. Rev.*, **64**, 104–  
1097 120, <https://doi.org/10.1016/j.quascirev.2012.12.008>.  
1098 Sugden, D. E., N. R. J. Hulton, and R. S. Purves (2002), Modelling the inception of the  
1099 Patagonian icesheet, *Quat. Int.*, 95 – 96, 55 – 64. DOI:10.1016/S0277-3791(01)00103-2  
1100 Sutherland, J. L., Carrivick, J. L., Gandy, N., Shulmeister, J., Quincey, D. J., and Cornford, S. L.:  
1101 Proglacial Lakes Control Glacier Geometry and Behavior During Recession. 2020.  
1102 *Geophys. Res. Lett.*, 47, e2020GL088865, <https://doi.org/10.1029/2020GL088865>  
1103 Tarasov, L. and Peltier, R. W.: Impact of thermomechanical ice sheet coupling on a model of the  
1104 100 kyr ice age cycle. 1999. *J. Geophys. Res.-Atmos.*, 104, 9517–9545  
1105 Tozer, B., Sandwell, D.T., Smith, W.H.F., Olsen, S.C., Beale, J.R., Wessel, P. Global  
1106 Bathymetry and Topography at 15 Arc Sec: SRTM15+. 2019. *Earth and Space Science*.  
1107 6, 10, 1847-1864. <https://doi.org/10.1029/2019EA000658>  
1108 Tigchelaar, M., Timmermann, A., Friedrich, T., Heinemann, M., and Pollard, D.: Nonlinear  
1109 response of the Antarctic Ice Sheet to late Quaternary Sea level and climate forcing, *The*  
1110 *Cryosphere*, 13, 2615–2631, <https://doi.org/10.5194/tc-13-2615-2019>, 2019.  
1111 Toggweiler, J.R., Russell, J.L., Carson, S.R. Midlatitude westerlies, atmospheric CO<sub>2</sub>, and  
1112 climate change during the ice ages. 2006. *Paleoceanography and Paleoclimatology*. 21,  
1113 <https://doi.org/10.1029/2005PA001154>  
1114 Troch, M., Bertrand, S., Lange, C.B., Cardenas, P., Arz, H., Pantoja-Gutierrez, S., De Pol-Holz  
1115 R., Kilian, R. Glacial isostatic adjustment near the center of the former Patagonian Ice  
1116 Sheet (48S) during the last 16.5 kyr. *Quaternary Science Reviews*. 277.  
1117 <https://doi.org/10.1016/j.quascirev.2021.107346>  
1118 Yan, Q., Wei, T., Zhang, Z. Modeling the climate sensitivity of Patagonian glaciers and their  
1119 responses to climatic change during the global last glacial maximum. 2022. *Quat. Sci.*  
1120 *Rev.*, 288. <https://doi.org/10.1016/j.quascirev.2022.107582>  
1121 Zech, J., Terrizzano, C.M., García Morabito, E., Veit, H., Zech, R., 2017. Timing and extent of  
1122 late Pleistocene glaciation in the arid Central Andes of Argentina and Chile (22°-41°S).  
1123 *Geogr. Res. Lett.* 43, 697–718. <https://doi.org/10.18172/cig.3235>.  
1124  
1125  
1126